Three-Dimensional Crater Formation Measurements During Plume-Surface Interaction in a Reduced Gravity Environment

by

Trevor Crane

A thesis submitted to the Graduate Faculty of
Auburn University
in partial fulfillment of the
requirements for the Degree of
Master of Science

Auburn, Alabama
May 4, 2024

Keywords: Plume-Surface Interaction, Stereo Photogrammetry, Parabolic Flight, Drop Tower, Reduced Gravity

Approved by

David Scarborough, Advisor, Associate Professor, Aerospace Engineering
Brian Thurow, Professor and Department Chair, Aerospace Engineering
Vrishank Raghav, Associate Professor, Aerospace Engineering

Abstract

Plume-surface interaction experiments were conducted in a 4.27 m tall drop tower facility to achieve 0g conditions, where g is Earth gravity at $9.81\ \frac{m}{s^2}$. Following the drop tower experiments, Martian (0.38g) and Lunar (0.16g) gravity conditions were simulated via parabolic flight. A stereo photogrammetry technique was used to capture crater formation under these gravity conditions, allowing for the quantification of the effect of gravity on crater depth and volume evolution. Three nozzle heights of 25D, 40D, and 50D, where D is the nozzle exit diameter, and three nozzle pressures of 5, 10, and 15 psig were investigated using the drop tower at both 0g and 1g. Results from the 0g experiments were compared to the results obtained using the same nozzle heights and pressures under 1g. The results indicated that crater evolution occurred more rapidly during 0g conditions, resulting in deeper and wider craters compared to those formed under 1g. During the parabolic flight, five nozzle heights between 25D and 60D at 15 psig were tested. It was found that the trend of more rapid crater evolution with decreasing gravity followed for Lunar and Martian gravity.

Acknowledgments

Thank you to my friends and family. I would not have been able to finish this thesis without your endless support.

A tremendous thanks to my friend and colleague Daniel Stubbs for being able to troubleshoot any and all problems that occurred in the lab. Your guidance and dedication significantly contributed to the success of this project.

Thank you to my advisor, Dr. Scarborough, for giving me the opportunity to work on this research and go on the parabolic flights. I now know what it is like to get sick on the Moon, Mars, Earth, and in zero gravity.

Finally, I want to acknowledge everyone at the Auburn University Combustion Physics Laboratory and our internal PSI collaborators Vikas and Lokesh whose contributions played a part in the completion of this thesis.

This research was funded by NASA grant number 80NSSC21M0230. The technical point of contact for this project is Dr. Wesley Chambers at Marshall Space Flight Center. I would also like to thank Dr. Ashley Korzun at NASA Langley Research Center and Dr. James Mantovani at NASA Kennedy Space Center for their valuable feedback and discussions during this work. This work was completed in part with resources provided by the Auburn University Easley Cluster. The assistance of Mr. Andy Weldon in the fabrication of the experimental setup is gratefully acknowledged.

Table of Contents

List of Figures

List of Tables

Chapter 1

Introduction

The ability to accurately predict the effect of plume-surface interactions (PSI) is one of the most important obstacles to returning and operating on the Moon. As we plan to return to the lunar surface, it is essential to consider the risks posed by PSI. These risks include potential damage to surrounding hardware, existing structures, and the landing vehicle due to ejected lunar regolith. A dust cloud created from the ejected particulate may form, potentially obscuring view of the landing site. This phenomenon was observed during the Apollo lunar module landings [1]. As a rocket exhaust plume from a lander impinges onto the surface of a planetary body, surface erosion occurs resulting in the formation of a crater and high-speed ejection of particulate. An example of PSI affecting hardware was when the Apollo 12 Lunar Module landing caused a small amount ejected regolith to pitt the paint on the Lunar Surveyor III. The observed damage on the Surveyor is notably less severe than expected, indicating that it likely encountered only scattered fringes of the ejecta, sparing it from extensive damage, but it would have been orders of magnitude worse if the Surveyor caught the brunt of the spray [2]. To properly mitigate these risks, it is important to understand the interaction between the lander's exhaust plume and the surface including effects such as crater and ejecta cloud formation and evolution. Current experiments at Auburn University Combustion Physics Laboratory are focused on simulating reduced atmospheric and reduced gravity environments. This thesis focuses on the effect of reduced gravity conditions on PSI.

The observed crater evolution process is a result of surface erosion caused by the interaction between an exhaust jet and the surface. This erosion process is affected by the weight of the particles, with heavier particles tending to resist erosion. Further, the geometry of the crater

is affected by the weight of the particles in the surrounding particle bed. A heavier particle bed is more prone to avalanching effects and the particles require more momentum from the flow to move. Metzger et al. found that particle entrainment depended directly on the momentum flux of the jet and was indirectly proportional to the particle weight [3–7]. Inspired by the seminal work of Metzger et. al., an initial dimensionless analysis for the ratio of the aerodynamic force to the particle weight yields eq. 1.1, which represents the cratering and particle entrainment effectiveness of the exhaust, where T is the nozzle thrust, A is the nozzle exit area, ρ_p is the particle density, ρ_f is the fluid density, d_p is the particle diameter, and g is gravity

$$\theta_T = \frac{Aerodynamic\ Forces}{Particle\ Weight} = \frac{\frac{T}{A}}{(\rho_p - \rho_f)gd_p}. \tag{1.1}$$

In this study, stereo photogrammetry is used as a non-intrusive measurement technique to yield time-resolved, 3-D, full-domain experimental data on crater evolution for reduced and Earth gravity conditions. Gravity is expected to play a critical role in determining the erosion rate and geometry of the resulting crater, as gravity directly affects the weight of a particle [8, 9]. To gather quantitative reduced gravity data for PSI, a drop tower was constructed at the Auburn University Combustion Physics Laboratory (AUCPL). Concurrent with the drop tower experiments, a facility was designed and constructed for conducting reduced gravity experiments on parabolic flights. The drop tower was used to conducted experiments in 0g, and the parabolic flights were used to conduct experiments in Lunar and Martian gravity. The reduced gravity data obtained by these studies can be used to support the development of scaling laws to predict PSI behavior.

Chapter 2

Background

PSI was originally researched during the Apollo missions, as it was a critical obstacle during Lunar landings [10]. During the landings, there was regolith entrainment caused by landing module's retrorocket plume, which obscured the surface during touchdown. Gene Cernan, whom was an astronaut for the Apollo 17 mission, was quoted saying during the technical debrief: "I think dust is probably one of our greatest inhibitors to a nominal operation on the moon. I think we can overcome other physiological or physical or mechanical problems except dust." [11]. These observations of the PSI problem highlights the importance of understanding and mitigating potential PSI effects during future missions.

The Apollo 11 mission report stated, "surface obscuration caused by blowing dust was apparent to 100 feet and became increasingly severe as the altitude decreased" [12]. This observation corresponded to about 52 seconds before touchdown. During the final descent in several of the Apollo missions, the rocket exhaust from the landing module caused minimal to zero visibility of the landing site due to dust [10]. During the Apollo 12 mission, the visibility from the pilots point of view was zero at an altitude of about 50 feet, and he relied entirely on his instruments for landing cues [13]. Lack of visibility poses significant risks to the landing module. Any malfunction or failure of these instruments could jeopardize the mission's success. Additionally, the formation of craters during the landing process, caused by the plume of the lander's retrorocket eroding the regolith surface, presents further challenges. Depending on the size and characteristics of these craters, there's a potential risk of the lander being unable to safely touch down without the threat of tipping, thereby complicating the landing procedure.

The Apollo 12 mission report first described the mechanism causing the erosion during the Apollo 11 and 12 landings as viscous erosion. This phenomenon occurs when the jet plume exerts a shear stress on a regolith surface, causing the regolith particles to be moved. These particles get entrained in the momentum of the jet and transported across the surface. Roberts developed a theory for viscous erosion for lunar dust [14–17], where he describes the mechanism as "a transfer of radial momentum from the flow to the surface layer of the dust" [17]. It was noted during the Apollo 12 mission that "the shearing force of the gas picks up weakly cohesive particles, injects them into the stream, and accelerates them to high velocities" [13]. The altitude of first erosion and the transport rate were able to be correlated to many characteristic parameters such as engine chamber pressure, Mach number, material density, particle size, and cohesion [13]. These parameters such as, particle size and density [5, 18–20], cohesion [21–24], nozzle heights [25–28] are still evaluated in current studies with the intention to develop scaling relations. After the Apollo missions, Romine et al. looked into the parameters that affect PSI. They investigated experimentally and analytically the interference of the Viking retrorocket exhaust plume impingement on the Martian surface. They tested different nozzle configurations, and it was determined that the conventional bell nozzle configuration would produce extreme disturbances to the landing surface, so alternate nozzle configurations were to be explored [29]. Although these experiments were to improve the Viking lander engine, the results could be used to inform the design of other retrorockets as well. Another early study by Alexander et al. experimented with stationary and horizontally moving jets to better estimate crater dimensions over a variety of jet and regolith conditions. These tests were run at various nozzle heights, angles, and velocities over flat simulant beds under ambient atmospheric pressures and temperatures [30]. From this study, it was found that if the jet surface pressure exceeded a "critical value," cratering would result from an "explosive failure" of the material. This "explosive failure" can be defined as the bearing capacity failure of the material bed. A more recent study [20] notes that bearing capacity will continue until the crater is slightly deeper than the core length of the jet, after which viscous erosion becomes the dominant cratering mechanism.

A few of the first optical diagnostic tests for PSI were conducted by Norman and Conner, which used an X-ray technique to measure crater growth in a bed of glass beads up to a depth of 15 cm. Norman and Conner conducted experiments to investigate the applicability of the erosion relations developed by Roberts[14–17]. Their experiments scaled length, time, and mass specifically for the Lunar Module [31]. Land and Clark continued these experiments and investigated the effect of the jet impingement in a vacuum environment with various particle sizes and nozzle heights [32]. Craters formed in non-cohesive material have steep walls and avalanche at jet cut-off into a more conical shape. Land and Conner observed diffused gas crater eruption following nozzle shutoff [31] in the case of smaller particles, which exhibit lower porosity. Diffused gas eruption occurs due to the accumulation of subsurface gas pressure. Scott and Ko were the first to experimentally look into the porosity of different particle beds with a wider distribution of particle sizes. They concluded that the porosity of the material contributed to the process of particle ejection from the crater. Gas that permeated into the soil during the jet flow, flowed upward and out of the soil at the end of firing [33]. Diffused gas eruption poses a potential hazard to landing vehicles as the gas eruption will entrain and eject particles toward the lander. Land and Clark's studies concluded that there is a certain height at which the nozzle plume will not erode the surface, and that height varies with surface particle size [32].

Many more recent PSI experiments were conducted using a splitter plate [5, 19, 25, 34–36] to be able to see a 2-D cross section of the crater during the crater formation process. This setup includes a box containing a granular material, typically a select size of sand, silica, or glass beads. One side of the box is optically accessible, with a beveled edge. The nozzle exit is positioned above the beveled edge to have half of the jet impinging on the granular surface. A high speed camera records the 2-D cross section of the crater formation through the panel. The panel is either illuminated with a laser sheet through the panel or a light source directed toward the box. Image processing techniques can then be used to extract crater geometry from the crater cross-section profile. The downside of using a splitter plate, is that it is inherently an intrusive measurement technique. The plate induces boundary layer formation and particle deposition that may effect cratering dynamics. The data is also limited to extrapolating the

2-D cross-sectional crater profile to a 3-D crater. This assumes a symmetrical crater, which does not hold true for smaller, cohesive material beds [37] or reduced atmospheric pressure conditions [27].

Haehnel et al. first used a subsonic jet with a splitter plate style experiment to show whether crater depth is influenced by the permeability of the bed material. They used three particle diameters ranging from 134 μm to 6 mm and densities from $0.9g\ cm^{-3}$ to $2.65g\ cm^{-3}$. Crater growth was documented by capturing still images of the crater during the test. Geometry information was obtained using edge detection algorithms available from the Matlab Image Processing Toolbox [19]. They were able to estimate crater sidewall slope and crater depth as a function of jet strength. The derived relations can predict final crater depth as well at the time it takes to reach maximum depth for subsonic jets as a function of the impinging flow and particle properties. Three different nozzle inner diameters were used. They found that the crater geometry can be predicted in terms of an erosion parameter that includes the effects of bed permeability [19].

A non-intrusive measurement technique, which has been used in flow diagnostics [21, 38–40], is planar laser-induced fluorescence (PLIF). PLIF uses a laser to excite a particular species in a flow, which produces fluorescence from the excited molecules. Considering an experiment aiming to visualize density gradients in a fluid, brighter regions in the images correspond to higher species concentrations, indicating denser regions in the flow field. The flow can then be imaged to visualize flow structures in jets and obtain quantitative flow properties [38]. Tyrrel et al. used this technique to investigate the flow features caused by the intrusion of a splitter plate. They observed flow features that attach to the splitter plate and turbulent wall jet features that could effect the dynamics of the granular media [38]. Korzun et al. will use PLIF in one of their physics focused ground test campaigns to gather impingement profiles on a flat plate and quantitative flow visualization data [21]. However, this technique is so far limited for PSI experiments by being coupled with splitter plates, yielding 2D erosion profiles.

Another non-intrusive measurement technique that has been recently used for PSI experiments is stereo photogrammetry. Stereo photogrammetry has previously been used in experiments to obtain a set of digital elevation models of soils to analyze surface roughness changes

of soil due to rainfall [41]. A similar study by Tran et al. used the stereo technique to analyze the roughness of soil samples in erosion tests to a higher accuracy [42]. Recently, the stereo photogrammetry technique was utilized to for PSI research as a non-intrusive measurement technique to obtain 3D measurements of the PSI induced crater. It was first used to measure PSI cratering experiments by Stubbs et al. in Earth atmospheric pressures at multiple, stationary nozzle heights [26]. In these experiments, the synchronized stereo cameras captured the crater growth at 1000 Hz at 2560 x 1600 pixel resolution. This method to quantitatively define crater geometries was further developed to be used with reduced atmospheric experiments [27] and reduced gravity experiments [28]. These experiments used the semiglobal matching stereo method [43, 44] to calculate the disparity map from the image pairs. This technique requires a semi-unimpeded view of the crater geometry to properly identify particle locations. For that reason, the stereo method is useful for calculating crater geometries from point clouds during the initial crater growth. As the crater develops and ejects material, view of the crater gets increasingly obstructed, leading to errors. This will be discussed more in Section 4.2.

The effects of reduced atmospheric pressures on the crater formation process is another important parameter to understand to create models for Lunar or Martian missions. Reduced atmospheric pressures has been investigated in previous experiments using vacuum chambers [21, 25, 27]. Gorman et al. conducted splitter plate experiments in a large cylindrical vacuum chamber at NASA Marshall Space Flight Center. Their experiments varied nozzle height of a sonic nozzle [25]. They concluded that gas and granular properties do not affect power laws associated with crater depth growth, they only affect the initial erosion rate and the critical transition time, where critical transition time is the time at which crater growth transitions to a sublinear regime. They also show that the initial erosion rate scales with nozzle pressure ratio [25]. Stubbs et al. similarly tested the effects of various nozzle heights using a sonic nozzle inside a vacuum chamber, but used the stereo photogrammetry technique[27]. Stubbs et al. found that the crater geometry significantly changed for reduced atmospheric pressures. Their experiment shows that for some nozzle heights at sub-atmospheric conditions,

a unique lobed crater geometry was observed that was not observed under atmospheric conditions. The differences in crater geometry was attributed to the nozzle plume at the surface being highly under-expanded resulting in wider and shallower craters and slower erosion [25, 27].

Gravity plays a significant role in the development of craters and ejecta dynamics due to PSI. Since the weight of the particles decreases in reduced gravity, the force required by a plume to erode a particle bed is lower. Therefore, all other parameters constant, a reduction in gravity would result in more rapid crater formation. The densimetric Froude number can be used to relate gravity to crater erosion, $Fr = \frac{u_e}{\sqrt{\frac{\Delta\rho}{\rho} g \bar{d}}}$, where g is gravity $\Delta\rho$ is the difference in gas and solid particle densities, $\bar{d}$ is the particle diameter, and u_e is the jet velocity [18, 21, 35, 45]. The Froude number can be interpreted as the ratio of the inertial forces acting on a particle within a flow field to gravitational forces keeping particles together. This relationship is often expressed as the ratio of dynamic pressure to the weight of the particle. A higher Froude number suggests that a particle is more influenced by its inertia. Therefore, in situations with decreased gravity, erosion rates may increase due to the increased dominance of inertial forces over gravitational forces.

Drop towers are one of the most straightforward methods of attaining 0g. Prior drop tower experiments have examined PSI induced crater formation in low pressure and reduced gravity environments with glass beads, steel beads, and sand [8, 46]. Kuhns et al. utilized a drop article that could be pulled to a vacuum and the pressure difference between the drop article and ambient atmospheric pressure drove the flow through the nozzle. Using this apparatus, Kuhns et al. found that reduced atmospheric craters were small with a central uplift whereas craters formed under reduced gravity were wider and deeper. Similarly, Chambers et al. observed that PSI behaviors are significantly more pronounced at reduced gravity conditions, and reducing the nozzle height increases the amount of material ejected from the crater [8]. Baba et al. conducted a microgravity experiment using a drop tower to validate a coupled CFD-DEM analysis to reproduce the scattering behavior of sand particles and crater growth. They used a silica particle as the regolith simulant with a average particle size of 0.525 mm. They dropped a vacuum chamber with an attached vacuum buffer chamber. The buffer chamber was used to reduce the pressure rise during a test. Inside the chamber, their experiment was set up with a splitter plate

illuminated by a laser sheet and a high-speed camera to capture the cratering behavior [36]. Measurements from this experiment were qualitative, and they observed the differences in the crater growth between 1g and 0g using the drop tower and the CFD-DEM analysis. Nevertheless, traditional drop tower experiments are limited only to 0g conditions, where there is no traditional application for PSI. Landing surfaces are associated with planetary bodies that have some level of gravity; even asteroids have microgravity that effect particle ejection [47]. Regardless, drop tower experiments are a good way to isolate the effects of gravity for numerical model validation and make qualitative observations and preliminary measurements.

Parabolic flights can help satisfy the shortcomings of the drop tower experiments by being able to achieve any reduced gravity condition. The flights also provide much longer reduced gravity time compared to the drop towers. Several experiments have used these parabolic flights to research the effects of reduced, zero, and greater than Earth gravity [9, 20, 22, 23, 47–51]. Most commonly, these flights target Lunar conditions, Martian conditions, and zero gravity. The flights provide the acceleration conditions for up to 30 s during the parabolas. Between parabolas, there is a 20 sec 1.8g phase as the plane reaches the trough of the parabolic trajectory. Larger experiments are usually bolted to the cabin floor of the aircraft while smaller experiments may be free floating. For PSI Experiments that are bolted to the floor, the regolith may experience residual accelerations of 0.01 -0.02g [47].

Immer and Metzger conducted one of the first PSI experiments on the parabolic flights using a small splitter plate [34]. Their experiment was conducted in a sealed 12 in x 8 in box, and they recorded video of the tests at 640x480 resolution at 8 Hz. They investigated the effects of regolith compaction, crater formation properties, and angle of failure as a function of of gravity. The material bed was reset after each test by picking up and tilting the box. They were able to conclude that craters become much larger in reduced gravity, and the asymptotic behavior of craters are unaffected by compaction [34]. Brisset et al. describes two experiments, PRIME [47] and COLLIDE [51], where they impacted centimeter-sized sized projectiles in a regolith simulant. They observed that at a given impact speed, more mass was ejected during microgravity conditions compared to reduced gravity, but the average ejecta speed was lower [22]. This correlation between gravity and ejecta speed translates to PSI as the impact

speed of a solid object is analogous to the bulk momentum of nozzle flow. The crater formation due to a solid body impact into a regolith surface may relate to early crater growth during PSI if the jet exceeds the bearing capacity of the regolith. Both scenarios result in momentum transfer to disrupt the regolith surface and create a crater.

Parabolic flights are extremely useful for gathering reduced gravity data, especially for Lunar and Martian conditions, as small fluctuations in gravity will not adversely affect the data as it may for zero gravity. However, if the microgravity condition needed to be accurate to 10^{-4}g for asteroid landing conditions, then the fluctuations may pose an experimental problem [52]. Despite this, some asteroid g-level experiments have been successfully conducted at 0.05g [47]. While in reduced gravity, there is still a downward force that helps lock particles together, and increases their inter-particle forces due to friction that resists particle movement and ejection [22]. Brisset et al. noticed, during their impact experiments, that particles with higher cohesion allow for a partially elastic response during an impact, leading to a rebound in the projectile [22]. For a jet impinging on a regolith surface, this phenomenon would likely result in higher resistance to erosion.

It is useful to couple drop tower experiments with the parabolic flights. A drop tower is a cheaper way to test prototype facilities and inform design decisions for the flights. Heißelmann et al. used a prototype of this experiment in a drop tower using ambient pressure and temperatures with larger particles before maturing the experiment for the reduced gravity flights. Other experiments have used the parabolic flights to investigate collisions of fragile millimeter sized particles in a vacuum chamber at low velocity and temperature. [48, 50]. Drop towers may be a better way to reproduce steady 0g conditions than parabolic flights, but its difficult to achieve a perfect 0g level. As a result of the difficulties in conducting experiments at precise microgravity conditions, numerical simulations are currently being used to simulate these extremely low gravity conditions [52].

Despite the experimental work investigating PSI, numerical models are necessary to fully replicate Lunar or Martian conditions. There have been several studies that used modeling and simulation to investigate PSI cratering [1, 5, 36, 53]. Accurate models and simulations

are important to apply the theoretical observations and scaling relations of PSI to more complex configurations. Since we are unable to fully recreate the Lunar or Martian environments on Earth, simplified Earth-based experiments can control which parameters we change. From these experiments, models can be used to extrapolate and couple these controlled parameters. Experiments are necessary to provide data to validate these models. Non-intrusive experiments that do not introduce complex flow phenomenon are more ideal to validate models. Metzger et al. conducted and validated CFD experiments based on corresponding splitter plate experiments. They found that material ejected from the crater can either escape the crater or be recirculated through a cratering mechanism called diffusion-driven shearing [5]. This shearing occurs beneath the tip of the crater where gases are stagnant, but is coupled with viscous erosion, which occurs over the rest of the inner crater. They also conclude that the crater growth reaches an asymptotic state when the rate of sand ejected equals the rate of sand recirculated [5].

Metzger et al. developed scaling relations between erosion rate and gravity during their parabolic flights [9, 20]. During their flight campaign, there were three gravity conditions, several particle sizes, and different gas velocities that were the main parameters of interest for these flights. They proposed that the depth scaling of the crater depth growth rates could be described with the function $d = a\log(bt+1)$. Where a is the depth scale and b is the time scale. This led to the associations that $a \propto H$ and $b \propto \rho v^2 D/H^\alpha$, where H is the nozzle height, ρ is the jet density, v is the jet velocity, and D is the inner nozzle diameter. Guleria and Patil also observed that the temporal growth of the crater depth follows this logarithmic function [35], and Gorman et al. followed up with these scaling relationships, under Earth gravity, by developing a scaling transition model between early and late stage crater growth development. Early stage crater evolution follows a linear relationship with time where the growth is directed primarily toward crater depth, and that late stage crater evolution follows a 1/3 power law [25]. With this model, it is suggested that gas and granular properties do not affect these power laws for crater growth. It was also shown that the initial erosion rate scaled with nozzle pressure ratio.

Along with the logarithmic function, an arctangent function was also used to describe the crater depth growth [18, 26, 54]. This function has the form $D = a\tan^{-1}(b(t^c))$ where a, b, and c are curve fitting coefficients. The arctangent function was shown to predict the

long-term crater growth better than the logarithmic fit [18, 26]. With this function, the depth asymptotes to $0.5a\pi$. Other experiments were able to identify two cratering regimes when using subsonic jets [5, 25]. These scaling parameters and curve fitting coefficients were studied experimentally [5, 25, 26] and with Computational Fluid Dynamics [5, 55]; However, they do not consider the effect of gravity. Many of these correlations have not been verified to hold in reduced gravity environments.

Another scaling study by Yamamoto et al. looked at the formation and collapse of transient craters under Earth gravity to see how crater size scales with various impact parameters. They proposed scaling relations for impact crater sizes. These relations include a gravity-scaled pi-term (from pi-group scaling), defined as: $\Pi = 3.22ga/v_i^2$, where g is the gravitational acceleration, a is the projectile radius, and v_i is the impact velocity [56]. If a correlation between the object-impact cratering and PSI cratering is confirmed, this gravity scaling relation could be be applied to early crater development due to PSI.

This section has provided context into the current state of understanding the PSI phenomenon. The research started during the Apollo era when there were concerns regarding the impact of regolith on landing visibility and potential damage to spacecraft and infrastructure. Present-day research often relies on intrusive measurement techniques, such as splitter plate experiments, to qualitatively analyze cratering dynamics, often under the assumption of symmetrical cratering. Techniques such as stereo photogrammetry allow for non-intrusive, full-domain 3D measurements of cratering phenomena. Also, scaling laws have not been fully developed nor validated for reduced gravity conditions. This thesis proceeds to detail experiments employing stereo photogrammetry to assess and quantify the impact of reduced gravity on PSIs using a drop tower and parabolic flight facility. To confidently draw conclusions about scaling relations regarding reduced gravity, and to obtain more quantitative data, a non-intrusive, full domain experiment is ideal.

Chapter 3

Methods

3.1 Drop Tower Experiments

3.1.1 Drop Tower

The drop tower facility was constructed inside the Combustion Physics Laboratory at Auburn University. The facility had a rectangular profile that stood 4.27 m tall with a 1.52 m x 1.52 m base. A rendering of the drop tower facility is shown below in Figure 3.1. The framing of the tower was constructed from 15 series t-slot aluminum framing. Foam padding was layered at a height of 30.5 cm at the bottom of the tower to absorb the impact of the drop. During the initial testing of this facility, less foam padding was used. This resulted in the on board computer powering off upon impact. In addition to the foam padding on the ground, a layer of foam was added under the computer on the drop article to prevent damage during the drops. A winch was attached to the bottom of the drop tower frame via mounting plate. The drop article was lifted by a 1/8 in stainless steel cable attached to the winch, and a two-pulley system guided the cable around the top of the tower and back down to the drop article. An electromagnet was attached to the end of the winch hook, allowing for the drops to be initiated by cutting power to the electromagnet. Double-wide t-slot framing was used for beams that the pulleys are attached to resist deflecting. A 3D printed cable guard was installed over the central pulley to prevent the cable from ejecting from pulley due to the recoil of the electromagnet release.

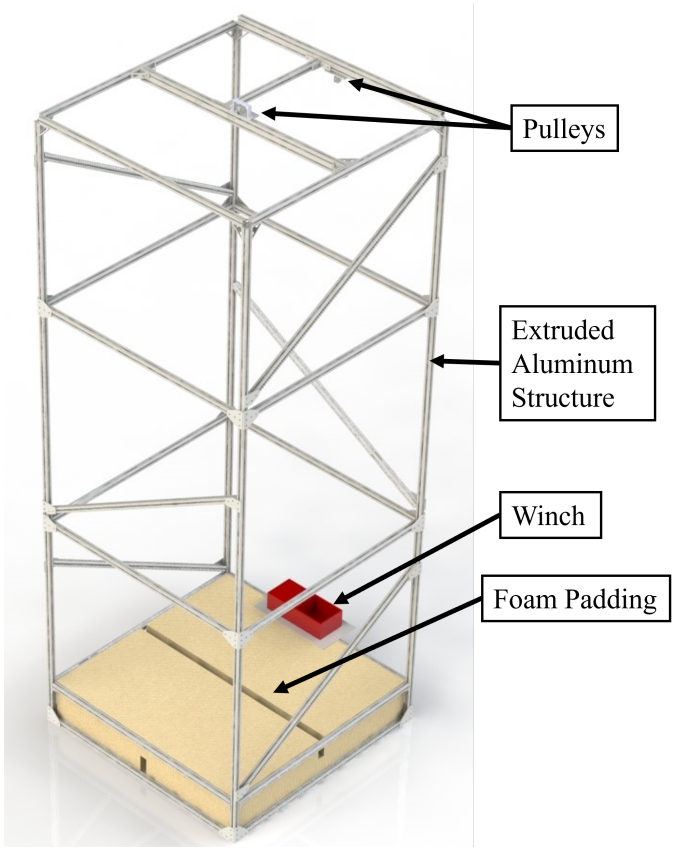

Figure 3.1: Drop Tower Rendering

Fig. 3.2 shows the typical acceleration felt by the drop article during an untethered drop test. The y-axis is the acceleration due to gravity, felt by the drop article, and the x-axis is the time in seconds. There is a solid black reference line to show 1g at $9.81m/s^2$ and a dashed black line to show the target 0g condition. For the purpose of this paper, "0g" is used interchangeably with micro-gravity, as there is usually some amount of jitter or perturbation around 0g. The drop is initialized at time $t = 0$. The small spike before the deceleration is from the recoil as the experiment is released. The drop article decelerates to 0g after approximately 0.15 s. The acceleration data in Fig 3.2 was smoothed using a moving average algorithm in Matlab. It shows that there was approximately 0.6 s of 0g during a drop. Following the 0g section, the two large spikes and subsequent oscillations on the graph are from the initial impact and bounces of the drop article landing as it settled on the foam padding. Although 0.6 s of test duration is subjectively a short time, previous crater formation experiments using the stereo photogrammetry technique [27, 57] have shown that plenty of useful data on crater formation can be acquired during the drop window.

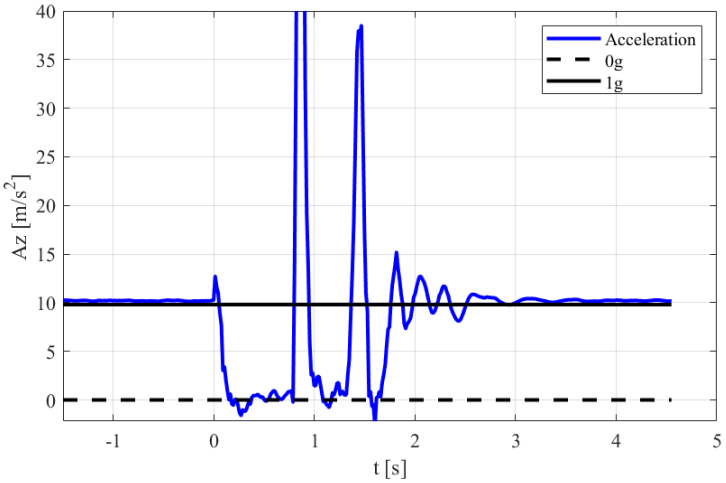

Figure 3.2: Drop Article Acceleration vs. Time

The accelerations for the drops were recorded using an MPU6050 accelerometer. The MPU6050 measures the accelerations and radial velocities in the x, y, and z directions as well as temperature when powered on. The range of the accelerometer was set to measure $\pm 2g$, but it is capable of measuring up to $\pm 16g$ if needed. The MPU6050 connected to an ESP32 micro-controller and outputs acceleration data over I2C. This ESP32 development board has an micro SD card slot, and the accelerations are written to the card at roughly 40 Hz. The data is comma-delimited to easily read and use in MATLAB.

3.1.2 Drop Article

The drop article, shown in Fig. 3.3, is an optically accessible cylindrical vacuum chamber that is 425 mm diameter x 470 mm height. However, for the drop experiments mentioned in this paper, ambient atmospheric pressure was used. The chamber is enclosed in t-slotted aluminum framing, which supports poly-carbonate panels that hold all the electrical equipment. The experimental equipment mounted on the drop article allows for an isolated untethered drop. All on-board components are powered by two 24 V lithium ion battery packs. One battery pack is used to power the LED lights inside the bucket, providing 168 W. The other battery pack is used to power the rest of the electronics such as the solenoid, pressure sensor, DAQ (Data Acquisition) system, on-board computer, and cameras. A high level device schematic is shown in Fig. 3.5. Fig. 3.5 shows the hardware/ electronics that were mounted to the top of

the drop article bucket. Two 24 V rechargeable, lithium-ion, batteries were used to power all devices. The on-board computer powers the DAQ, accelerometer, and both cameras over USB at 5 V. The on-board computer was an Intel NUC and was controlled over WiFi via remote desktop by a computer not attached to the drop article. Through the NUC, the two Allied Vision Alvium 1800 U-158m cameras and drop parameters were initialized using a LabVIEW script. A NI6001 DAQ triggers the camera recordings and opens the solenoid at the start of the drop. The compressed air cylinder is refilled after every test to a storage pressure of 120 psig. There was a voltage regulator to drop down the 24 V from one of the battery packs to 19 V to power the on-board computer. The battery packs typically lasted for about two to three hours of testing.

The drop article had a steel plate attached to the top of the extruded aluminum framing that the electromagnet attached to. While the electromagnet was attached to the drop article structure, it pressed down on a switch button. When the power supply was turned off to the magnet, the electromagnet disconnected and the switch was released. This was the start of the drop. The signal from the opening switch was monitored by the DAQ system. When the DAQ saw the switch open, it started the test by opening the nozzle solenoid and triggering the image acquisition sequence from the cameras. This operation was controlled by a LabVIEW code running on the on-board computer. All the other hardware was attached to polycarbonate mounting plates that were attached to the lid of the t-slotted frame; these components were secured to the plate by either bolts or zip ties. The structural lid of the drop article was designed so that it could be opened and closed with all hardware remaining attached.

The pair of Allied Vision cameras have an aperture of f/5.6 and focal length of 8 mm and were used to acquire stereo image pairs at a 1.6 MP resolution of 1456 (H) x 1088 (V) at a frame rate of 150 Hz. The cameras were positioned 40 cm above the sand surface and oriented with a viewing angle of 4.2° relative to vertical. The exposure time of each camera was set to 500 μs. The stereo camera pair was mounted in line with the nozzle exit and captured images of the crater for the full duration of the test. LED light strips were attached to the inside of the test article to provide 168 W of illumination. Several rows of these light strips were wrapped around the inside circumference of the bucket as well as on the acrylic lid for top down illumination.

The nozzle stagnation pressure was controlled via a pressure regulator upstream of the solenoid valve. There were two pressure regulators in series are in place to act as a dual stage regulator and minimize the effects of pressure drop in the air storage tank on the delivery pressure to the nozzle during testing. This allowed for a constant outlet pressure as the supply pressure in the compressed air cylinder drops during the test. A solenoid valve directly upstream of the nozzle was used to remotely control the start and stop of nozzle flow. A pressure transducer was mounted directly upstream of the nozzle to monitor the exit nozzle pressure during testing. The digital output of the sensor was 0-10V, which corresponded to 0-100 psi.

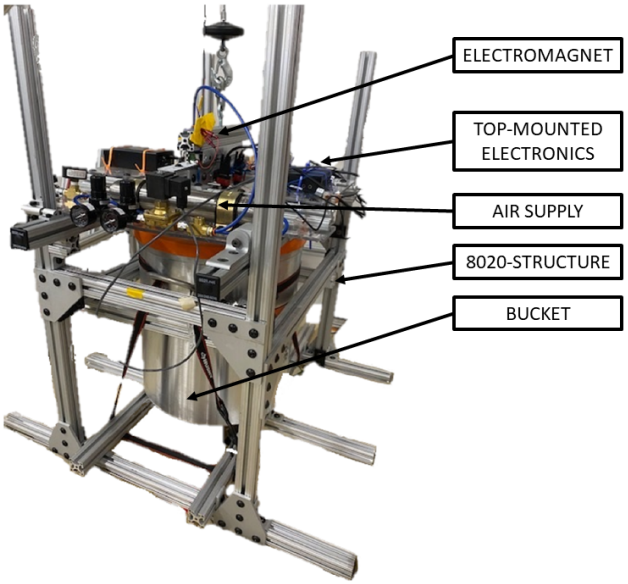

Figure 3.3: Drop Article Schematic

A high level overview of a drop test was illustrated in Fig. 3.4, which showed the labeled components in the cross section of the drop article bucket. At a set nozzle height, measured in nozzle diameters from the sand surface, a plume impinged on the sand bed. This resulted in crater formation and sand was ejected from the rim of the crater. The gas jet was provided from the mounted compressed gas cylinder and used compressed air. The air exited through a sonic nozzle with a constant inner diameter of 4.93 mm. This resulted in flow with a Mach number at or below $M = 1$ at the exit of the nozzle depending on the nozzle pressure. The nozzle was securely mounted to a nozzle positioning system at fixed elevations above the lunar simulant bed with care being taken to ensure that the nozzle was orthogonal to the simulant bed and that

the nozzle does not shift in its mounts during drops. Sand was selected as the regolith simulant for the drop experiments to easily compare to our existing ground data. The sand particle sizes were 600-850 μm. At this size, the sand is effectively cohesionless. This means the sand does not stick to itself during the crater formation process and will leave a more uniform crater.

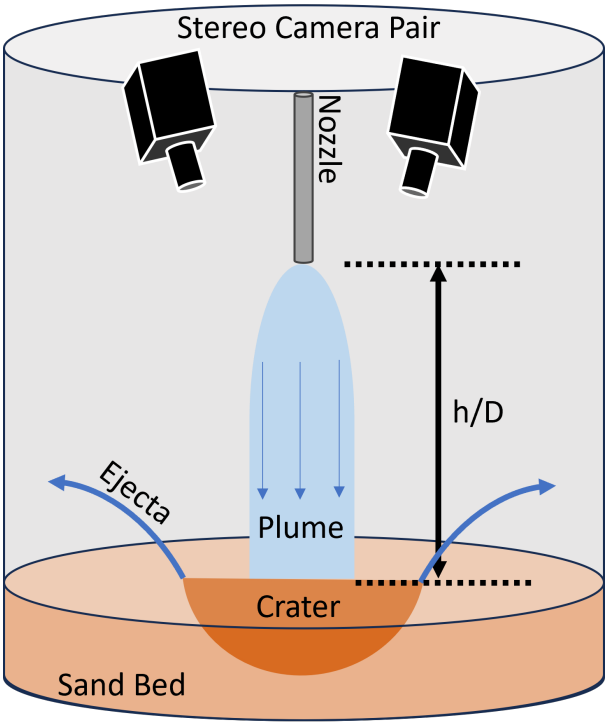

Figure 3.4: Drop Article Bucket Cross Section

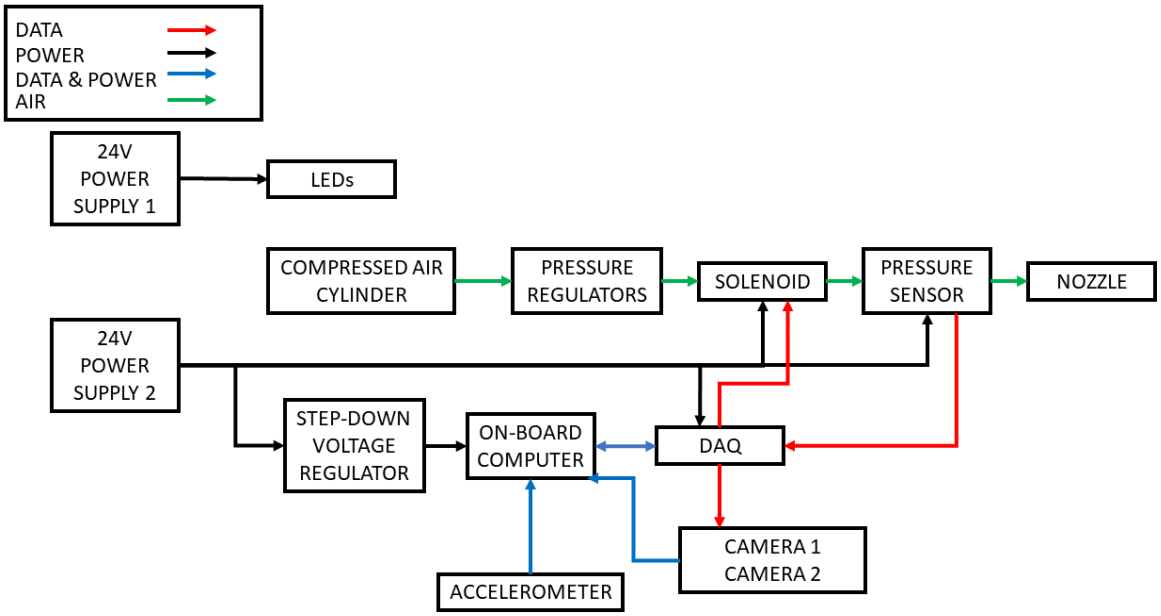

Figure 3.5: Drop Article

3.1.3 Drop Tower Test Matrix and Parameters

The drop tower experiments covered three nozzle heights: 25D, 40D, and 50D. These nozzle heights were chosen because 50D was the highest achievable height for the current drop article configuration, and 25D was the lowest nozzle height at which crater information was retained for at least 150 ms. For each nozzle height, three nozzle pressures were tested: 5 psig, 10 psig, 15 psig. These three pressures were chosen to determine which pressure would be optimal for future parabolic flight experiments. Each ground and drop test was repeated three times so the repeatability of the results could be assessed. The test matrix is shown below in Table. 3.1.

Table 3.1: Test Matrix

Nozzle Height (D)	Nozzle Pressure (psig)	Gravity Condition (g)
25	5	0 & 1
	10	0 & 1
	15	0 & 1
40	5	0 & 1
	10	0 & 1
	15	0 & 1
50	5	0 & 1
	10	0 & 1
	15	0 & 1

Table 3.2 shows the experimental parameters that were constant for all tests listed in Table. 3.1. The test duration was set at 1 s so that the nozzle flow remains on for the entire duration of the drop. The sand bed depth was chosen to be 4 in. This depth was tested to be sufficient to prevent the nozzle flow boring to the floor of the test article during testing. Adding more sand is unnecessary as it would just increase the mass of the drop article, which would increase the risk of damage when landing.

Table 3.2: Experimental Parameters

Test Duration	1 s
Nozzle Diameter	4.93 mm
FPS	150
Camera Resolution	1.6 MP
Sand Bed Depth	4 in
Sand Particle Size	650-800 μm

Table. 3.3 shows the thrust generated by the drop article depending on the nozzle pressure. For each nozzle pressure case, there is a corresponding mass flow rate through the exit of the

nozzle. The mass flow rate was $0.00205\frac{kg}{s}$, $0.00312\frac{kg}{s}$, and $0.0041\frac{kg}{s}$, for the 5 psig, 10 psig, and 15 psig nozzle pressures respectively. The calculation for thrust considers standard temperature and pressure ambient conditions, and takes into account Fanno flow effects. The Fanno flow calculation is estimated using a 24 in length duct and a friction factor of 0.007. The following Fanno flow model was used to calculate the change in mach number over the length of the tube.

The Fanno parameter can be defined as:

$$F_1 = \frac{4fL}{D}, \tag{3.1}$$

where f is the friction coefficient, L is the length of the constant area tube required to achieve supersonic flow, and $D = 0.194\ m$ is the hydraulic diameter of the duct. The Fanno parameter relates to the Mach number as,

$$F_1 = \frac{1 - M^2}{\gamma M^2} + \frac{\gamma + 1}{2\gamma} \ln(\frac{M^2}{(\frac{2}{\gamma+1})(1 + \frac{\gamma-1}{2}M^2)}). \tag{3.2}$$

where $\gamma = 1.4$ is the heat capacity ratio of air. The length required for the flow to choke, L^*, is:

$$L_1^* = \frac{F_1 D}{4f}, \tag{3.3}$$

Solve for L_2^*,

$$L_2^* = L_1^* - L. \tag{3.4}$$

The Fanno parameter at the exit of the tube, F_2 is:

$$F_2 = \frac{4fL_2^*}{D}. \tag{3.5}$$

If L_2^* is less than 0, the nozzle is choked and the exit Mach number is 1. To calculate the nozzle exit Mach number below choking, the "fzero" function was used in MATLAB. The exit velocity was calculated as:

$$v_{exit} = M_2 * a, \tag{3.6}$$

where a is the speed of sound in ambient conditions. Knowing the exit velocities, and considering Fanno flow effects, an accurate thrust for the drop article nozzle was calculated.

$$Thrust = \dot{m} v_{exit} + (p - p_0)A \tag{3.7}$$

where $\dot{m}$ is the mass flow rate through the nozzle p is the nozzle pressure, $p_0 = 101325\ Pa$ is the free stream static pressure, and $A = 0.000019\ m^2$ is the nozzle exit area.

Table 3.3: Drop Article Nozzle Thrust

Pressure (PSIG)	**Mass Flow Rate (kg/s)**	**Thrust (N)**
5	0.00205	0.811
10	0.00312	1.618
15	0.0041	2.429

3.2 Reduced Gravity Flight Facility

3.2.1 Flight Facility

The flight facility was constructed at the same time as the drop tower. A rendering is shown in Fig. 3.6. The flight facility framing was constructed out of 6105 T5 extruded aluminum. All the structural brackets used on the facility are also made of aluminum 6105 T5. The six structural wall panels are made of 0.5 in thick cast acrylic. The panel that all the electronics are mounted on is made of extruded polycarbonate. The mounting plates for the nozzle, linear actuator, and cameras are all aluminum 6061. The floor plates are all aluminum 7075 T6. The bolts holding on the structural brackets and the acrylic panels are made of 5/16" black-oxide coated

alloy steel and meet ASTM F835 and ASME B18.3 standards. The bolts used in the nozzle assembly are ¼" black oxide alloy steel. The bolts mounting the facility to the cabin floor are AN-6 Steel. All 5/16"-18 bolts and t-nuts used in the assembly were torqued to 12 ft-lbs. The material strengths can be referenced in the stress analysis document, which was provided to the parabolic flight provider, Zero-G. The frame dimensions (excluding the electronics on top and compressed gas tank assembly) were 46in x 46in x 49.5in. The methodology for conducting reduced gravity experiments and processing the crater data was identical to those used for the drop tower. Rectangular foam blocks are positioned at the bottom of the facility to restrict the sand bed to a 18" x 18" x 7" region at the bottom of the facility. These foam blocks reduced the amount of sand needed in the facility and acted as a reference level when resetting the sand. A linear translation stage was mounted to a 0.5" thick aluminum plate to reduce vibration and nozzle recoil during a test. A stainless steel nozzle with an inner diameter of 4.93 mm was attached to the linear translation stage. The nozzle exit was directed toward the center of the sand bed so that the jet impinged perpendicular to the sand surface. A stepper motor controlled the raising and lowering of the nozzle via the translation stage. Accordion-style bellows protected the internal rod of the translation stage from ejected sand during tests.

A 3D-printed glove port was mounted to one of the acrylic walls to allow for manual resetting of the sand surface between tests. A 30" rubber glove was hose clamped to the glove port to provide a sand-proof seal. Tethered to the inside of the glove port was a straight edge. The straight edge was secured under the glove port via Velcro. The straight edge was 26" long with a cone-shaped cross-sectional profile. It was 3D-printed around a stainless steel tube to stay rigid. It had a small hook at the end to better retrieve sand from the far corners of the facility. After each test the sand bed was smoothed and reset using the straight edge. Sand bed resetting occurred immediately after each test while still in reduced gravity, as it was easier to reset the bed in reduced gravity than hyper-gravity.

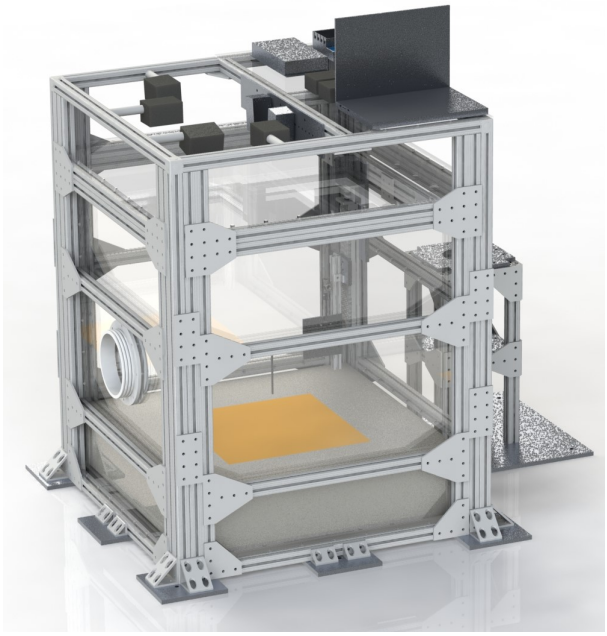

Figure 3.6: Parabolic Flight Facility

The compressed gas bottle assembly, shown in Fig. 3.7, held the 55 std. ft^3 bottle of compressed N_2. The bottle had a diameter of 7 inches and a height of 23.5 inches. The frame dimensions of the gas bottle assembly (base area being the floor plate) was 24in x 24in x 24in, Figure. The total dimensions of the main flight facility and bottle containment when bolted together in the aircraft cabin were 65in x 46in x 49.5in. The bottle was pressurized to 2000 psig. The regulator mounted to the bottle had a 3000 psi max inlet pressure, and a 125 psi max outlet pressure. Downstream of the regulator, there was a 150 psig relief valve as well as a manual relief valve to prevent over-pressurization of the system. A solenoid valve was used to start and stop nozzle flow during the tests. The solenoid was controlled via relay module on the DAQ.

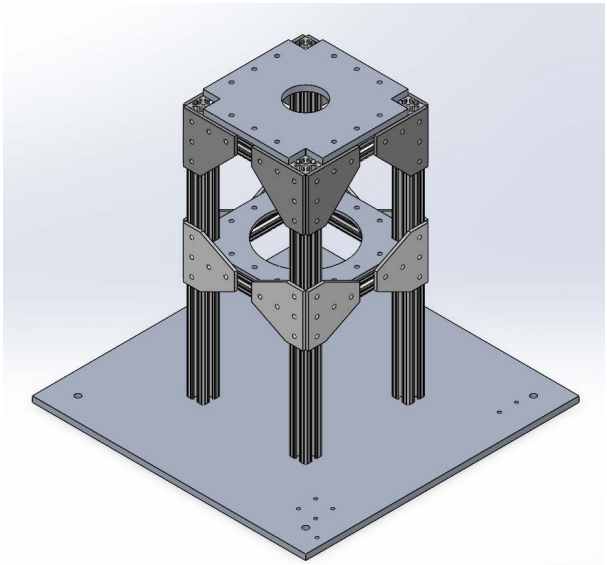

Figure 3.7: Compressed Gas Bottle Assembly

The stereo cameras were a set of Lucid Vision ATX051S-MC that captured images at 500 FPS at 5 MP resolution of 2448 (H) x 2048 (V). They have an aperture of f/8 and a focal length of 16 mm. The cameras were mounted 6.5" apart from each other and directed at an angle between $4\,\mathrm{deg}$ and $6\,\mathrm{deg}$ toward the sand surface. The angle of the cameras were not specific, as the slight variations were accounted for during the calibration. The crater images from the parabolic flights were captured at a higher frame rate and resolution than the drop tower experiments. The cameras each require a 10G Ethernet adapter, which connects to the laptop thunderbolt ports. An accelerometer was used to measure the gravity levels during each test. The accelerometer was made from an ESP32 micro-controller connected to a MPU6050 accelerometer. The ESP32 also connected to a BMP280 pressure sensor to record the cabin pressure. The flight facility DAQ comprised of a four channel chassis with a NI 9482, NI 9205, and NI 9402 module. The NI 9482 was the relay module, controlling the power for the solenoid. The NI 9205 was the analog input module for the nozzle pressure. The NI 9402 was a digital input/output module signaling the start trigger for the cameras. Four Multi-LED QX lights were mounted to the top of the flight facility aimed toward the sand surface. Each LED module produced 12000 Lumen and had a power draw of 150 W.

Power for the flight facility is provided from the aircraft power supply. NEMA 5-20 (20 Amp, 120 VAC) was provided for the flight. The power strip connecting the AC components

had a 15 Amp fuse, and the 24 VDC power supply had a 3 amp fuse for surge protection. There was a switch on the power strip that could act as an emergency stop to cut power to the experiment. The electrical box contains the 24V DC power supply that provides power to the 24V rail. The 24V rail powers the two cameras, the solenoid valve, the pressure sensor, and the stepper motor controller. A wiring diagram for the flight facility is shown in Fig. 3.8. The USB devices such as the ESP32 and RS485 (stepper motor communication) are powered through the laptop.

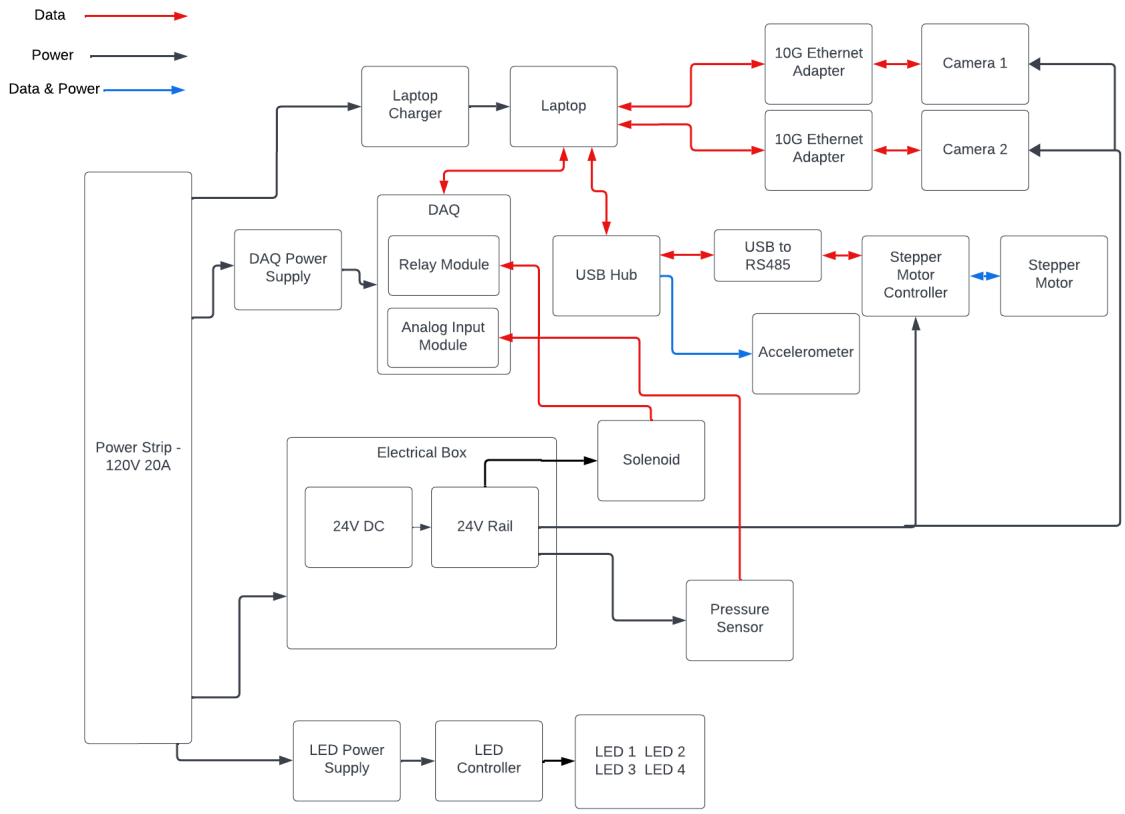

Figure 3.8: Flight Facility Wiring Diagram

3.2.2 Parabolic Flight Test Matrix

The test matrix for the first parabolic flight covered five nozzle heights at four gravity conditions. This test matrix is shown in Table. 3.4. The five nozzle heights cover 25D, 35D, 45D, 55D, and 60D. Based on the preliminary drop tower experiments, it was determined that 25D was the lowest nozzle height that may produce meaningful data, but lower nozzle heights may

be considered for future flights. The 60D maximum nozzle height was chosen as it is currently the upper limit of the linear translation stage, given a 25D minimum. Each of these nozzle heights were tested twice at each gravity condition. The four gravity conditions include Lunar (0.16g), Martian (0.38g), zero (0g), and hyper (1.8g). The main gravity conditions of interest were Lunar, Martian, and zero. Hyper gravity was added to the test matrix because it was possible to test with the current flight facility configuration, and was briefly covered in a previous study [20]. The hyper gravity condition did not get covered for all of the nozzle height, multiple repetitions due to concern about flier fatigue and nausea from operation of the facility under increased gravity.

Table 3.4: Parabolic Flights - PSI Test Matrix

	Lunar		**Martian**		**Zero**		**Hyper**	
	Test 1	**Test 2**	**Test 1**	**Test 2**	**Test 1**	**Test 2**	**Test 1**	**Test 2**
25D								
35D								
45D								
55D								
60D								

The flight facility experimental parameters are shown in Table. 3.5. The nozzle configuration used for the flights was the same as the drop tower's nozzle - with a 4.93 mm constant diameter nozzle. The test duration was chosen to be 2 s, as any crater formation beyond 2 s would be obscured by the ejected particles. This was determined from the drop tower experiments, as many of the craters became obscured after 0.5 s. However, Lunar and Martian conditions allowed for crater parameters to be calculated for a longer duration than on the drop tower as a result of the crater formation from the higher gravity conditions. A sand bed depth of 7 inches was used because the longer duration tests could bore the crater deeper than what was measured during the drop tower experiments. The current sand bed depth was not chosen

to be deeper due to weight considerations, but could be changed for future flights by modifying the foam inserts at the bottom of the facility. The particles used for this experiment were 650-800 μm diameter sand grains which were also used in the drop article.

Table 3.5: Flight Facility Experimental Parameters

Test Duration	2 s
Nozzle Diameter	4.93 mm
FPS	500
Camera Resolution	5 MP
Cabin Pressure	11.9 psia
Nozzle Pressure	30 psia
Sand Bed Depth	7 in
Sand Particle Size	650-800 μm

3.2.3 ZeroG Requirements

The flight facility was designed to adhere to ZeroG's Payload User Guide to satisfy and complete a Payload Integration Package (PIP). Along with the PIP, ZeroG required: a hazmat declaration listing, battery details and certifications, risk index and expanded task analysis, and safety data sheets for our compressed gas and sand.

A section within the ZeroG payload integration package is a stress analysis document outlining, in great detail, all components of the proposed facility, their material properties, and calculations for several load conditions that could potentially be endured during a flight. The ZeroG Research Payload User Guide outlines these requirements. The G-loading specifications that the flight facility required are as follows: 9 g's in the forward, aft, down, lateral, and upward directions with a factor of safety of 2 or higher. Load cases for the smaller components (less than 8lb) were conducted using a force gauge. The factor of safety for the larger structural components are determined by the tensile and shear strength of the structural brackets and bolts. The factor of safety for the floor plates and brackets are calculated with FEA using MSC NASTRAN/ PATRAN.

3.3 Stereo Photogrammetry

The stereo photogrammetry technique used by Stubbs et al. [26, 27], was adapted for this study to process the crater geometry data for reduced gravity conditions for both the drop tower experiment as well as the parabolic flight facility. The data obtained from reduced gravity experiments were analyzed to obtain 3-D, time-resolved images of the crater resulting from the exhaust plume-surface interaction. The stereo camera images were processed to produce a 3-D point cloud, which was then be analyzed to obtain the crater depth evolution, crater radius evolution, and volume evolution.

The stereo photogrammetry technique used a pair of synchronized monochrome cameras to capture image pairs. Monochrome cameras were used because they are typically able to absorb more light and have better resolution than color cameras. Color images from non-monochrome cameras require a color filter array or bayer filter which overall may reduce the resolution of the image. This is due to the grid of red, green, blue color filters that allows light at that particular wavelength to fall on a single pixel. Color cameras require a demosaicing algorithm to process the image by interpolating this filtered grid. So, if a sand particle happened to be a wavelength outside of a filter's spectrum, it would not be captured. A color filter array may also introduce false color artifacts into the image which could make results less accurate. In general, colored cameras are unnecessary for this application and would reduce accuracy and add more complexity.

The cameras for the drop article were calibrated using a checkerboard pattern, and the flight facility cameras were calibrated using a charuco pattern. The checkerboard, shown in Fig. 3.9, is comprised of a grid of 15 mm squares. The calibration procedure included taking 30 images at 1 frame per second of the checkerboard pattern while simultaneously moving the patterns around the field of view (FOV) manually. This calibration pattern was used to calibrate the drop article for the drop tower experiments. For best calibration results, at least 10 image pairs should were taken. Images were removed if they were blurry or if the pattern was more than 45 deg tilted from the camera plane.

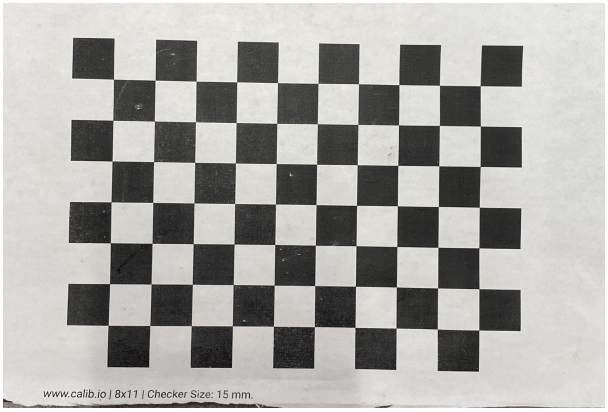

Figure 3.9: Checkerboard Pattern

The stereo camera calibrator app in MATLAB in the image processing and computer vision toolbox used the sets of checkerboard images to determine camera parameters such as distance to the region of interest and distance between the cameras. The stereo calibrator detects the corners of the checkerboard and attempts to re-project their locations. The app will also determine the mean pixel error.

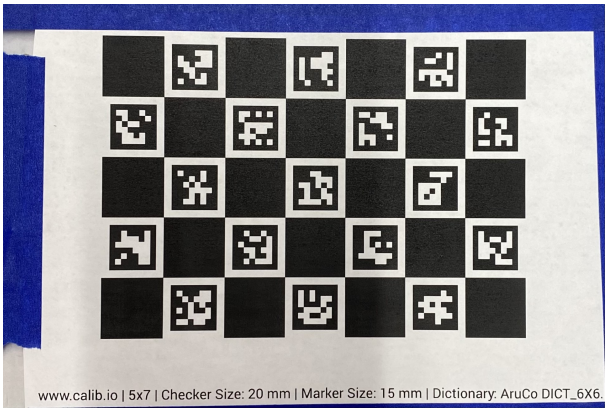

Figure 3.10: Charuco Pattern

Fig. 3.10 shows a charuco calibration pattern, which uniquely identify the corners independent of the other corners. Corner Detection is used to get points in the real world whose measurements you already know. This is useful for experiments where someone may be unable to remove an obstruction, such as a nozzle, during the calibration process. However, for the drop tower experiments, the checkerboard pattern was used since it was easy to remove the nozzle for calibration. The charuco pattern was useful for the flight facility when the lid was

sealed and the nozzle was in the way during calibration. Using the Charuco pattern required using a Python-based Open CV program to extract calibration parameters.

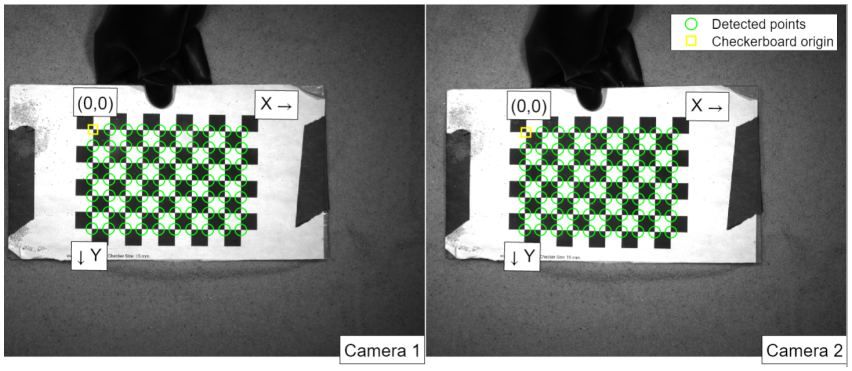

Figure 3.11: Corner Detection on Checkerboard

Fig. 3.11 shows the corner detection in the algorithm before the calibration. At the top of Fig. 3.11, there is a glove holding the calibration board on top of the sand surface. For the most robust calibration, the calibration board was manually moved around the camera's field of view. The green circles identify the intersections of the squares in the checkerboard pattern.

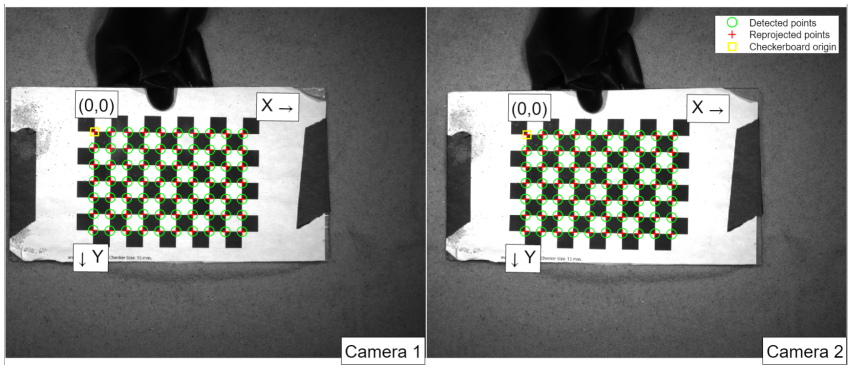

Figure 3.12: Re-projected points on Checkerboard

The re-projected points can be seen as the red crosses in Fig. 3.12, located at the intersection between the squares. The points in the checkerboard pattern are calculated relative to the origin, marked with a yellow square. The coordinates of the re-projected points are all positive values. The positive x direction is to the right of the origin, and the positive y direction is below the origin.

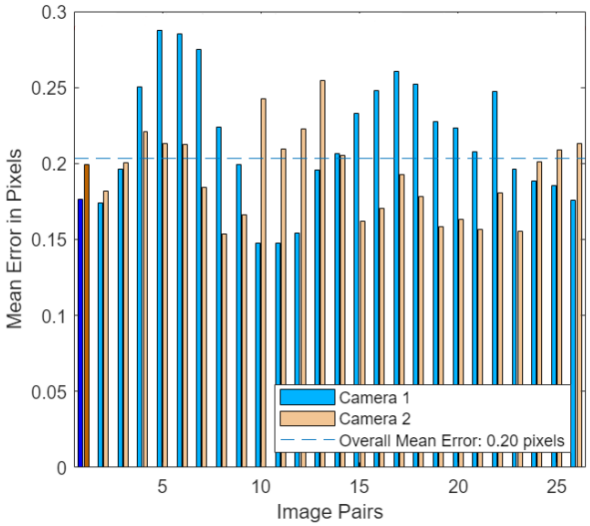

Figure 3.13: Re-projection Error

Fig. 3.13 shows a plot of the mean error in pixels vs the image pair for the two cameras. The y-axis shows the mean error in pixels, and the x-axis is the image pair number. This figure shows the mean error for both cameras as well as the overall mean. The mean error refers to the average error between detected points and reprojected points. The images used to create this plot were from the flight facility calibration session. The mean error calculated for this calibration was 0.2 pixels which translates to about 2 mm.

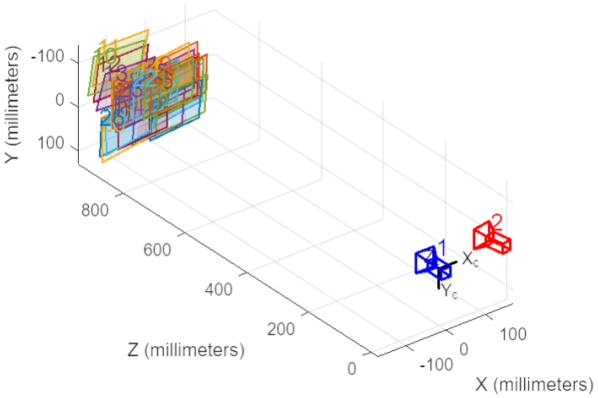

Figure 3.14: Camera Locations Relative to Calculated Image Pairs

Fig. 3.14 can be used as a sanity check for the calibration. It is used to see whether the cameras are approximately the correct distance apart from each other, and to see if the distance to the region of interest is realistic. Fig.3.14 shows the cameras approximately 800 mm from

the sand surface which is correct for the flight facility. The same camera calibration scheme was used for the drop article with similar values for re-projection error.

The image pairs, combined with camera parameters derived from stereo camera calibration, were input into a semi-global block matching algorithm. This algorithm seamlessly correlates each pixel in the left image with its counterpart in the right image. Subsequently, distance computation is performed for every pair of matching pixels. The resulting disparity map is created by representing these distance values as an intensity image. The disparity map is then used in a 3D reconstruction algorithm that generates a point cloud. By knowing the relative location of the cameras that took the image pair, features in the images can be matched. The points in these point clouds are associated with x,y, and z coordinates that can collectively be used to calculate geometric parameters about the crater. Crater depth is one of the crater properties that was extracted from the point cloud data, where depth was defined as the deepest 99th percentile of all points from the point cloud. The depth results referred to the absolute value of the depth relative to the surface plane. Positive depth values made it easier to compare across cases and other geometric properties. The crater volume. The crater volume was determined by integrating the depth of each point over the surface area of the crater. The extent of an induced dust cloud and visibility through the cloud are dependent on particle size and the depth of the dust layer [17]. By knowing the crater depth as a function of other parameters, one could model the effects of different landing conditions.

3.4 Camera Calibration and Accuracy

An accuracy assessment was conducted to evaluate the effectiveness of the drop article stereo imaging process. The accuracy of the stereo cameras for the drop article were determined by imaging a stair pattern of known step sizes. This stair pattern, shown in Fig 3.15, was 3D printed using a Ender 3 V2 Pro printer. The printing accuracy for the 3D printer is generally accepted to be within 0.1 mm. The individual step dimensions are 25.4 mm x 24.5 mm with a 5 mm step size. Spray glue was used to attach the 600-850μm sized sand particles to the stairs. The dimensions of the stairs were chosen to encompass the depth values that were typically seen from cratering in reduced gravity from preliminary tests. To assess the stairs

in the drop article, roughly 2 in of sand was removed from the bucket to encompass a more realistic measurement range of the crater. The sand bed was flattened at this new level before the stair pattern was placed in the bucket. This accuracy assessment, using the stair step pattern, was also successfully used in the flight facility as well as the AUCPL vacuum chamber facility.

Figure 3.15: 3D Printed Stair Pattern

The 3D printed stairs were placed in the drop article bucket within the field of view of both cameras. Only the top-down lights, mounted to the acrylic lid, were used during the imaging of the stairs. The side wall lights in the drop article bucket caused shadowing across some regions of the geometry, causing problems during post-processing, so they were turned off for the assessment. A longer exposure time of 2500 μs was used to compensate for the reduced lighting. The results of the accuracy assessment are shown in Table. 3.6 and Table. 3.7.

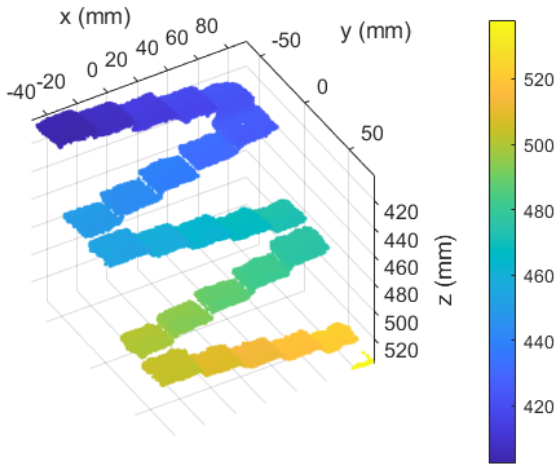

(a) Point Cloud of Stair Pattern for Drop Article

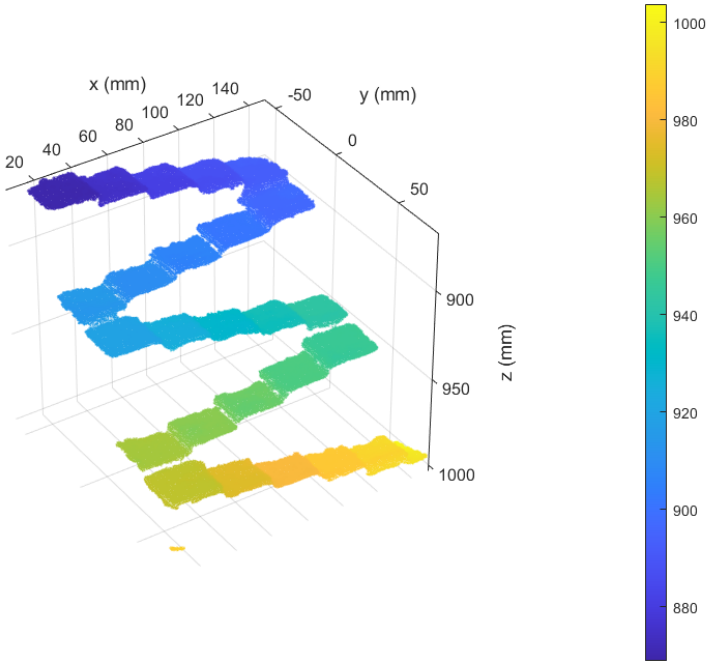

(b) Point Cloud of Stair Pattern for Flight Facility

Figure 3.16: Stair Pattern Point Cloud for Accuracy Assessment

Fig. 3.16 shows the point cloud reconstruction of the stair step pattern for the drop article, Fig. 3.16a, and the flight facility, Fig. 3.16b. A color gradient was used to visualize the steps at their respective heights. The mean step height in the direction of the cameras (z-axis) for the drop article was measured to be from 522 mm to 404 mm. For the flight facility, the steps

measured to be from 991 mm to 870 mm from the cameras. The region of interest had to be selected for each stair in ascending order, shown in Fig. 3.17a. The available points in each region are averaged together to provide a height for that step. The lowest stair was used as the reference height for the other stairs. This is why the heights listed for that step in Table. 3.6 and Table. 3.7 are either 0 or NaN.

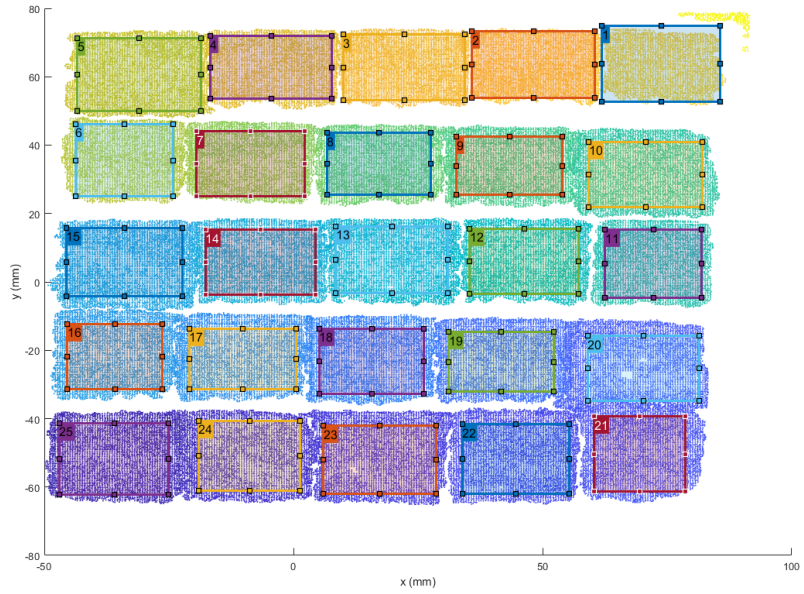

(a) Region of Interest Identification for Drop Article

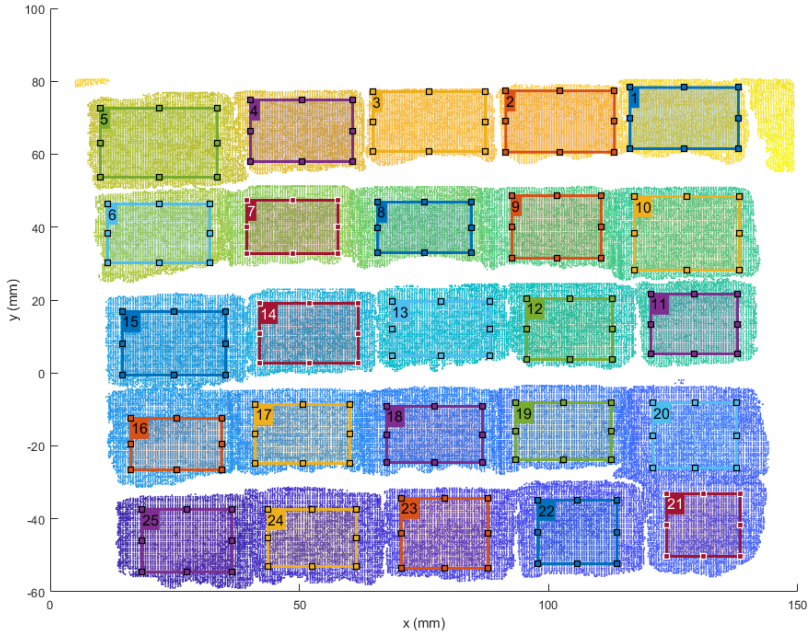

(b) Region of Interest Identification for Flight Facility

Figure 3.17: Region of Interest Identification for Stair Step Pattern Point Cloud

Table. 3.6 and Table. 3.7 show the actual height, reconstructed height, and absolute error for each of the stair steps from the point cloud for the drop article and flight facility respectively. The step number corresponds to the selected region of interest from Fig. 3.17. These values

are based on the points within the region of interest selected in Fig. 3.17. The absolute error is the difference between the reconstructed height and actual height. The percent error is the error between the calculated height and the actual height. For the drop article, the mean absolute error was 0.89 mm, the standard deviation of the absolute error was 0.73 mm, and the maximum absolute error was 2.75 mm. For the flight facility, the mean absolute error was 1.025 mm, the standard deviation of the absolute error was 0.87 mm, and the maximum absolute error was 3.15 mm. Since the mean error is approximately 1 mm and the absolute error for the lower and higher range of the stair pattern falls within the standard deviation, it is reasonable to conclude that the measured crater depth for both experiments is accurate to within at least 2 mm.

Table 3.6: Drop Article Accuracy Assessment

Step	Actual Height [mm]	Reconstructed Height [mm]	Absolute Error [mm]	% Error
1	120	118.823	1.177	0.991
2	115	114.122	0.878	0.764
3	110	109.492	0.508	0.462
4	105	104.802	0.198	0.189
5	100	99.968	0.032	0.032
6	95	96.111	1.111	1.170
7	90	90.340	0.340	0.378
8	85	84.473	0.527	0.620
9	80	78.282	1.718	2.148
10	75	72.284	2.716	3.622
11	70	68.964	1.036	1.481
12	65	63.908	1.092	1.680
13	60	59.138	0.862	1.437
14	55	54.528	0.472	0.858
15	50	49.782	0.218	0.436
16	45	46.013	1.013	2.250
17	40	40.317	0.317	0.792
18	35	34.426	0.574	1.640
19	30	28.254	1.746	5.819
20	25	22.253	2.747	10.987
21	20	19.073	0.927	4.635
22	15	14.249	0.751	5.004
23	10	9.549	0.451	4.507
24	5	4.109	0.891	17.811
25	0	0	0	NaN

Table 3.7: Flight Facility Accuracy Assessment

Step	Actual Height [mm]	Reconstructed Height [mm]	Absolute Error [mm]	% Error
1	120	120.701	0.701	0.584
2	115	116.125	1.125	0.979
3	110	110.086	0.086	0.079
4	105	104.414	0.586	0.558
5	100	98.278	1.722	1.722
6	95	94.150	0.850	0.895
7	90	89.928	0.072	0.080
8	85	85.519	0.519	0.610
9	80	80.488	0.488	0.610
10	75	76.356	1.356	1.808
11	70	72.473	2.473	3.533
12	65	66.551	1.551	2.386
13	60	60.432	0.432	0.720
14	55	54.826	0.174	0.316
15	50	49.077	0.923	1.847
16	45	45.138	0.138	0.307
17	40	40.339	0.339	0.847
18	35	36.364	1.364	3.898
19	30	31.410	1.410	4.701
20	25	26.896	1.896	7.584
21	20	23.154	3.154	15.768
22	15	17.398	2.398	15.989
23	10	11.731	1.731	17.314
24	5	5.145	0.145	2.896

Chapter 4

Results

The results in this section discuss both qualitative and quantitative effects of PSI induced cratering in reduced gravity environments. The drop tower was used first investigate the effects of micro- gravity on crater erosion. The parabolic flights followed the drop tower tests, allowing for the effects of Martian and Lunar gravity to be explored. The stereo-photogrammetry technique was implemented to non-intrusively observe and measure the crater crater erosion rates using both experimental facilities. The sets of stereo images were then processed to obtain crater geometric properties such as crater depth and crater volume. Curve fitting functions were applied to the drop tower depth data to predict long term crater growth rates and asymptotic crater depth. The parabolic flight results included discussions regarding environmental and experimental parameters that potentially influenced the consistency between tests.

4.1 Qualitative Observations

A qualitative assessment of the crater properties can be made from Fig. 4.1. This is a colored image of the crater taken from a GoPro video during a ground test at 1g (left) and drop test at 0g (right). The LEDs are shown wrapped around the inner perimeter of the bucket. Both tests used the same nozzle conditions at 12 psig at a nozzle height of 25D. The images are time synchronized, so the only difference in the crater formation is the gravity condition. Fig. 4.1 shows the craters right before the particles begin to obstruct the camera's view. Although the crater geometry information is unable to be obtained, these raw images files allow for a rough estimate of the crater radius even when the particles begin to recirculate with the jet. The 1g

crater diameter measured approximately 88 pixels and the 0g crater measured to be 235 pixels. The pixel measurements are indicated by the while line spanning the diameter of each crater. The diameter of the 0g crater measured to be 2.67 times that of the 1g crater. Overall, with all other conditions the same, the 0g crater is seen to be significantly wider and deeper, and the camera view becomes obstructed earlier than the 1g case. The camera's view of the crater was obstructed by the sand particles in Fig. 4.1 and is the reason why points within the crater cannot be reconstructed, such as in Fig. 4.4 (b).

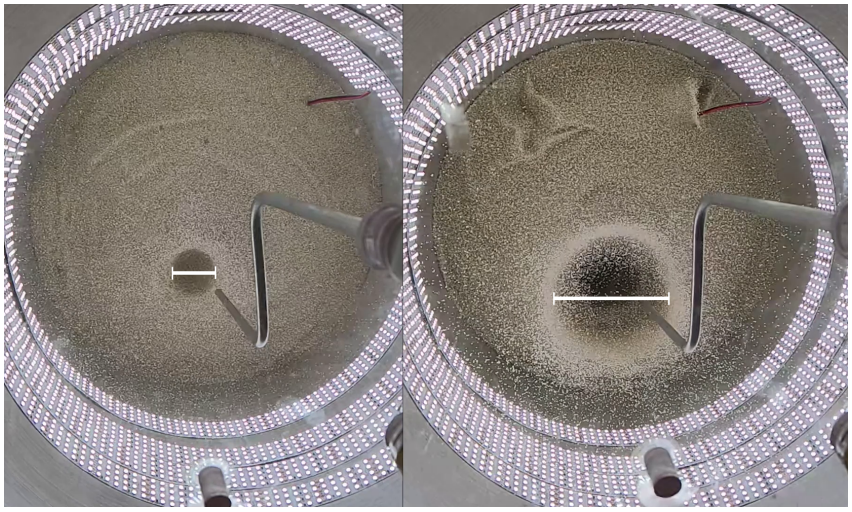

Figure 4.1: Crater Formation Seen by GoPro at 1g (left) and 0g (right), 12 psig Nozzle Pressure, 25D Nozzle Height

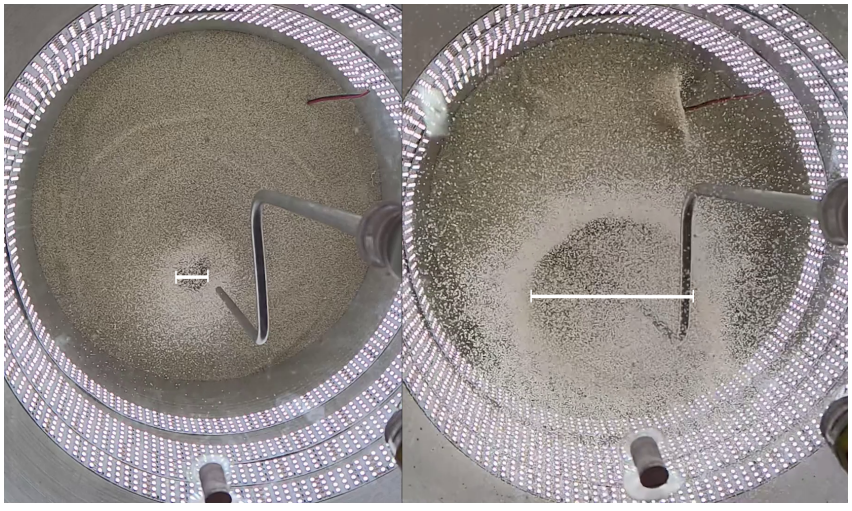

Figure 4.2: Obscured Crater Formation Seen by GoPro at 1g (left) and 0g (right), 12 psig Nozzle Pressure, 25D Nozzle Height

Fig. 4.2 are images from the same gopro sequence as Fig. 4.1 right before the end of the drop. It shows how both of the craters are obscured from the ejected particles, and demonstrates how the stereo cameras would not have optical access to reconstruct the geometry of the crater. The crater diameters from Fig. 4.2 are measured to be 66 pixels for the 1g crater and 350 pixels for the 0g crater. So, the diameter of the 0g crater at this time was 5.3 times that of the 1g crater, which means the difference in the crater diameter grows throughout the duration of the test.These dimensions were measured across the interior of the more dense particle region, which can be described as the more uniform light tan ring on the outside of the crater. Based on these final measurements, at the end of the drop, the diameter of the 0g crater was 5.3 times larger than the 1g crater. For the 1g case, crater diameter appeared to decrease as the nozzle flow continued; however, the ejected particles that began recirculating with the nozzle jet blocks the view of the crater edge. This same phenomenon happens for the 0g crater as well, except the dense particle region is much smaller relative the the crater diameter. If measured from the exterior of the dense particle sheet, the diameters were 160 pixels and 460 pixels for the 1g and 0g craters respectively. The thickness of this dense region is 37 pixels for the 1g crater and 55 pixels for the 0g crater. This increase is due to more material being ejected in a radial direction for the 0g case compared to the 1g case.

Differences in crater due to changes in nozzle height and nozzle pressure are shown in Fig. 4.3. These images were captured by one camera of the stereo camera pair on the drop article. Each image occurred at frame 50, which corresponds to 0.333 s after the beginning of the drop. Figs. 4.3a-4.3c are at a nozzle height of 25D, Figs. 4.3d-4.3f are at a nozzle height of 40D, and Figs. 4.3g-4.3i are at a nozzle height of 50D. The left column of images shows cratering from the nozzle at 5 psig, the middle column at 10 psig, and the right column at 15 psig. Fig. 4.3c shows the sand particles beginning to obstruct view of the crater. Meanwhile, Fig. 4.3g shows no visible crater.

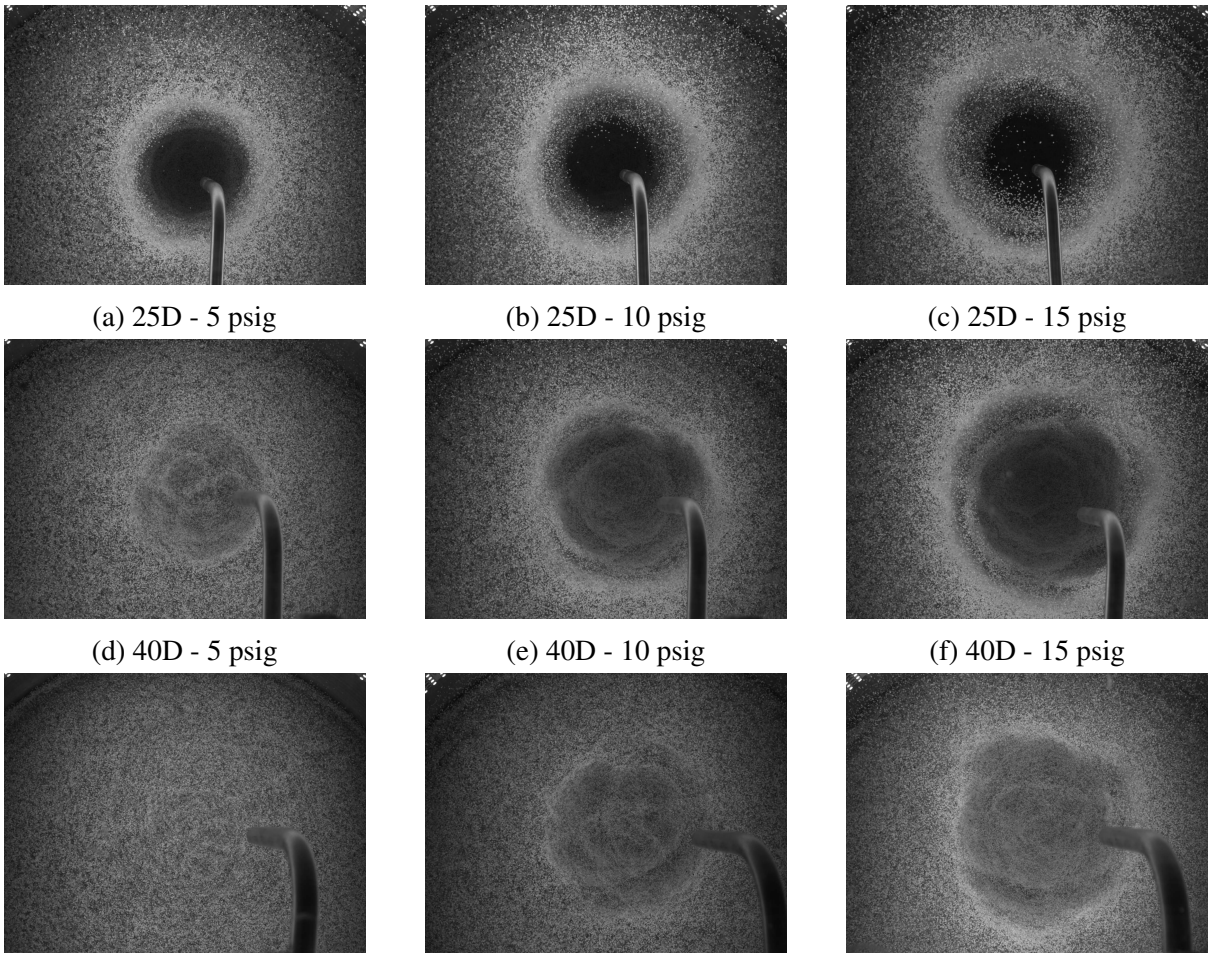

(a) 25D - 5 psig (b) 25D - 10 psig (c) 25D - 15 psig

(d) 40D - 5 psig (e) 40D - 10 psig (f) 40D - 15 psig

(g) 50D - 5 psig (h) 50D - 10 psig (i) 50D - 15 psig

Figure 4.3: Stereo Camera Perspective (One Camera) at 25D, 40D, 50D Nozzle Height and 5 psig, 10 psig, and 15 psig Nozzle Pressures at Frame 50 (0.333 s After Drop)

4.2 Point Cloud Data

To first verify the functionality of the drop tower facility, an initial case was tested with a nozzle height of 25D and a nozzle pressure of 15 psig at 0g. This case was chosen as it represents the most challenging case for reconstruction, i.e. the lowest nozzle height at the highest nozzle pressure with no gravity, which results in the most rapid crater formation. This translates to the highest surface force case with no force holding the sand in place. Furthermore, it was important to verify that the crater depth did not equal the sand bed depth. If crater depth matched sand bed depth, the drop article would have artificially limited the crater depth. Point cloud data from this case are shown in Fig. 4.4 (a) and (b). These point clouds indicate that the crater

does not bottom out within the bucket as the crater maintains a parabolic profile. These results also demonstrate that the stereo measurement methodology as implemented on the drop tower facility was able to successfully measure the crater geometry under 0g conditions. Additionally, the fact that the crater reconstruction was successful for the most extreme of the test conditions served as reasonable indication that the measurement methodology would succeed for the remaining test conditions.

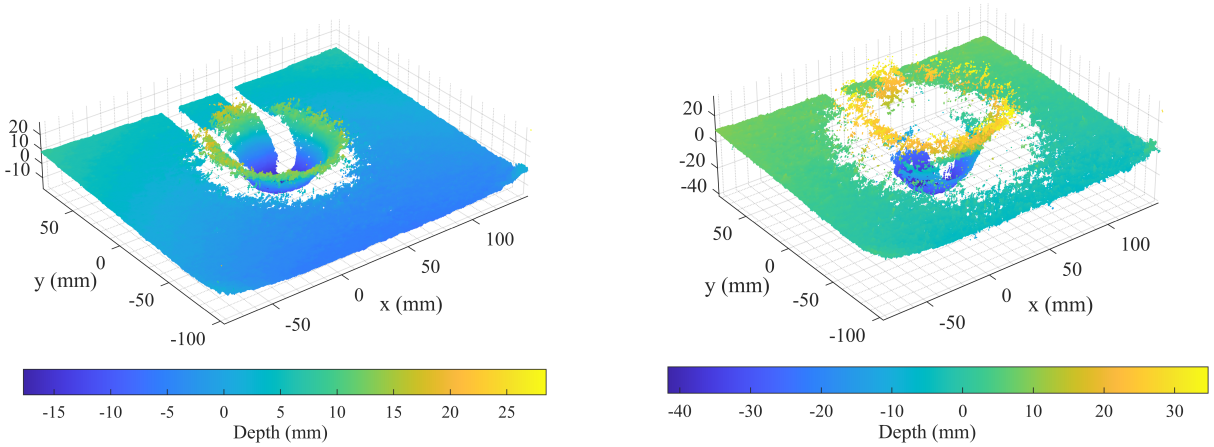

(a) Frame 15 (0.1s), Nozzle Height 25D, Nozzle Pressure 15 psig, 0g

(b) Frame 25 (0.167s), Nozzle Height 25D, Nozzle Pressure 15 psig, 0g

Figure 4.4: Point Clouds for Nozzle Height 25D at 15psi

The point clouds in Fig. 4.4 show the geometry of the crater at 0.1 s and 0.167 s measured relative to the start of the drop and initiation of nozzle flow. The two long sections without data in each image were from manually drawn masks around the nozzle to prevent the nozzle appearing as false data points. There are two nozzle shapes projected in the point clouds since there were different perspectives from both cameras. These masks are drawn around the nozzle for all point clouds for both the drop tower experiments as well as the flight facility experiments.

The x-axis and y-axis were measured in mm and define the plane of the sand surface in the bucket. The z-axis is the depth of the points in mm. The surface plane is defined by fitting a plane in the region of interest from the first point cloud file. The first point cloud shows the undisturbed surface as the plume does not yet reach the surface. The subsequent point clouds subtract the height of the surface plane from the depth coordinate of each point. There were slight imperfections about the zero reference level of the surface plane - more clearly

visible around the boundary of the point cloud. This is due to the method of resetting the sand bed perfectly flat with respect to the xy-axis. The edges of the bucket are more difficult to smooth out compared to the center region where the crater forms. Since the crater does not form near these boundaries, the data points are not influenced by any small discrepancy of the surface plane from zero. The lighter green and yellow points in both images represent particles that are pushed above the original surface level, and the darker blue points are deeper than the original surface level - representing the crater profile. Comparing the surface plane color between Fig. 4.4a and Fig. 4.4b, frame 25 is shown to have a lighter green color compared to the original blue color from the beginning of the test. This is due to the sand bed slightly expanding due to the particles no longer compacting from the force of gravity as well as potential micro-negative gravity conditions felt during free fall.

The point cloud quality rapidly degraded after ∼0.2 s for this case due to the ejected particles obscuring both camera's view of the crater. The depth reached 16 mm at frame 15 and reached 40 mm at frame 25. The ejected particles reached 16 mm and 30 mm above the surface for frame 15 and frame 25 respectively. As a result, characteristics such as depth and volume could only be extracted from the point clouds for so long as there is sufficient optical access to the crater. For all cases, data was shown until optical access to the crater was lost or until the end of the test, at 1 s.

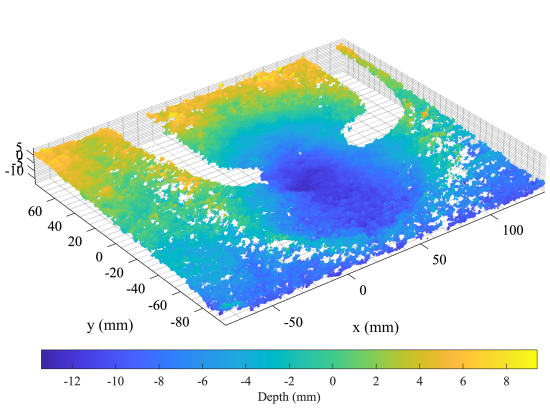

(a) Frame 45 (0.3s), Nozzle Height 50D, Nozzle Pressure 5 psig, 0g

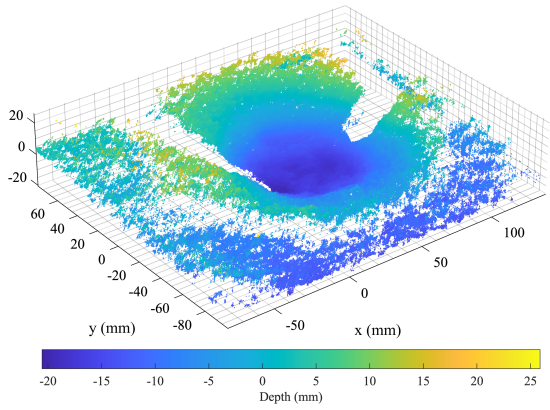

(b) Frame 90 (0.6s), Nozzle Height 50D, Nozzle Pressure 5 psig, 0g

Figure 4.5: Point Clouds for Nozzle Height 25D at 15psi

Fig. 4.5 shows the least dramatic case, at the highest nozzle height (50D) and the lowest nozzle pressure (5 psig). These figures use the same reference xy-axis zero level, and all axes are in mm. For this case, the depth reached approximately -10 mm at frame 45 and -20 mm at frame 90. However, the crater was not fully developed and was limited by the duration of the drop. Since the crater was not fully developed, the particle ejection was less significant; there was effectively no ejection seen in Fig. 4.5a, and minimal ejection in Fig. 4.5b, where particles reached a height of roughly 10 mm. Longer test duration would be needed to determine the maximum crater depth at these nozzle conditions. For this case, the crater size is almost the entire field of view of the cameras. For higher nozzle heights, a larger field of view may be needed to observe the full crater. Currently, the camera's FOV is slightly smaller than the drop article diameter. So, higher nozzle heights may require a larger drop article. A larger drop article would also reduce the amount of material bouncing off the walls back toward the crater.

The mask for the nozzle is larger and more far apart in Fig. 4.5 because the nozzle is closer to the cameras. Comparing Figs. 4.4 and Figs. 4.5, the surface looks more rough as these point clouds were from images longer into the drop. The surface roughness can be attributed to the slightly negative g's that were experienced during the free-fall, causing some of the particles to float toward the cameras. At these corresponding frames for the 25D, 15 psig case, the crater was completely obscured by the ejected particles. The sand bed was shown to fluidize and expand the longer it was in microgravity. Without gravity, there is no force compacting the sand, causing the bed to slightly expand from the microgravity perturbations. Similarly, the sand acted fluid-like due to reduced cohesion forces. In Fig. 4.5b, the cameras begin to have problems accurately measuring the particle locations on some of the surface.

4.3 Crater Geometry

4.3.1 Crater Depth

Fig. 4.6 shows depth vs time for all the drop article tests at 0g and 1g. The y-axis is the depth in mm and the x-axis is the time in ms. The solid lines represent the 0g cases and the dashed lines are the 1g cases and the colors match nozzle heights. The shaded region around any of the

lines is the standard deviation based on the three repetitions. The standard deviation was higher for the 0g tests compared to the 1g tests due to the inconsistencies of the drop. Inconsistencies could have included vibrations from the release mechanism and slightly different microgravity accelerations felt between tests. Fig. 4.6a, b, and c is depth measurements at a nozzle pressure of 5 psig, 10 psig, and 15 psig respectively. There is no 1g, 40D and 50D cases shown in Fig. 4.6a and no 50D case in Fig. 4.6b because there was no crater formation for those nozzle conditions. The jet did not have enough momentum to erode the crater.

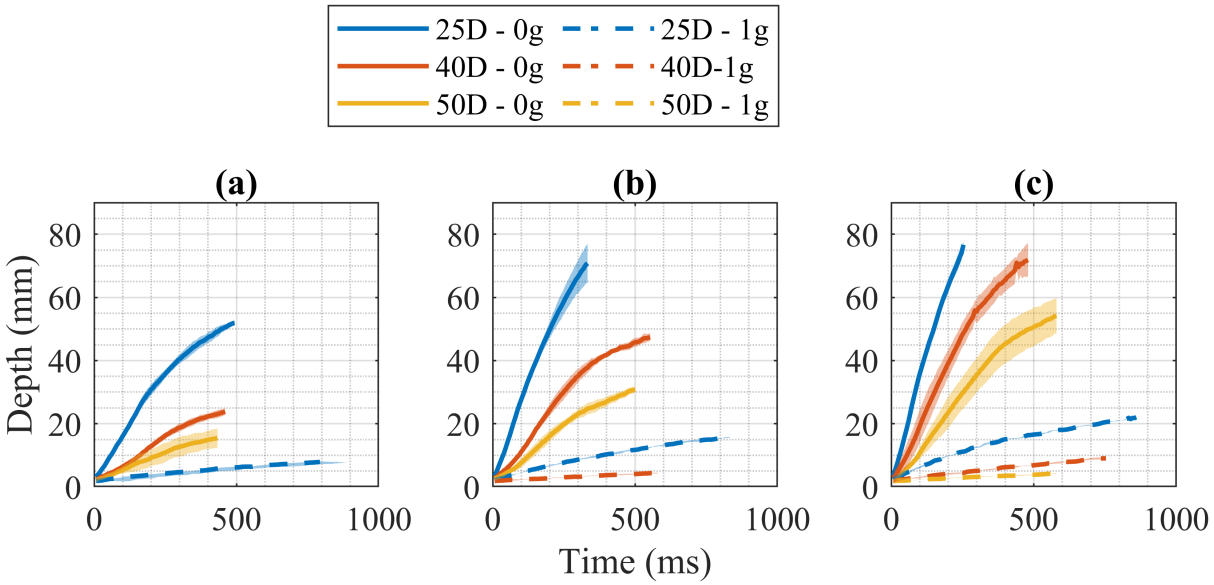

Figure 4.6: Crater Depth vs Time for Various Nozzle Heights at a Nozzle Pressure of (a) 5 psig (b) 10 psig (c) 15 psig

More easily seen with the 0g data, there is a region, typically within the first 100 ms, where the crater depth grows linearly. Then, the linear trend stops and the crater depth growth exhibits a decaying trend that appears to be approaching an asymptotic depth value. Previous works have observed this shift from linear to asymptotic crater growth [20, 25, 26]. However, for the current test duration, and due to the crater obscuration due to ejected particles, the asymptotic crater depth was unable to be measured using the stereo photogrammetry technique. The maximum crater depth can still be estimated using curve fitting functions and data from prior experiments in Section 4.4.

Table 4.1: Depth Comparison at Different Nozzle and Gravity Conditions at 400ms

Time (ms)	Nozzle Conditions	Depth at 1g (mm)	Depth at 0g (mm)
400	25D, 5psia	5.5	49.1
400	40D, 10psia	3.8	41.8
400	40D, 15psia	6.0	65.5
400	50D, 15psia	3.6	45.6

The crater depth is significantly larger for the 0g cases. Table 4.1 describes the effect of gravity on crater depth at 400 ms for specific nozzle conditions. At 400 ms, visibility for the 0g craters started to reduce and the crater growth slowed. The depth increased by an order of magnitude under 0g conditions. For example at 40D, 15 psia, the depth at 1g was 6.0 mm, and the depth at 0g was 65.5 mm. This is a 991.7% increase to the crater depth. Similarly, at 50D, 15 psia, the depth increased 1166.7% between the 0g and 1g cases.

4.3.2 Crater Volume

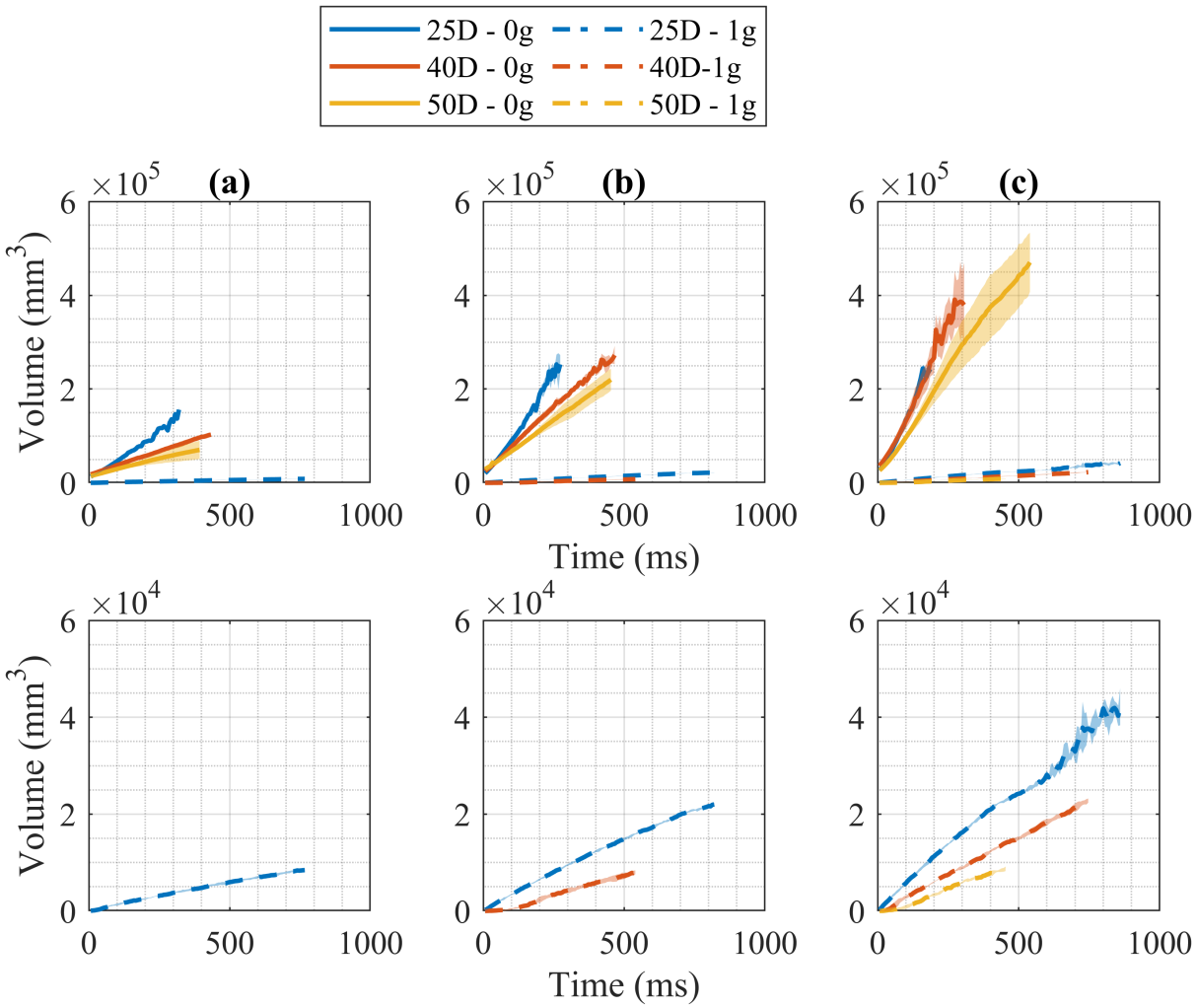

Figure 4.7: Crater Volume vs Time for Various Nozzle Heights at a Nozzle Pressure of (a) 5 psig (b) 10 psig (c) 15 psig

Figure 4.7 compares the crater volume measurement for the 0g and 1g condition for each nozzle height case. The results show that the crater volume growth rate increased with higher nozzle pressures and decreased with increasing nozzle height. The increase in crater volume growth rate with nozzle pressure can best be seen across Fig.4.7a, Fig.4.7b, and Fig.4.7c for the 50D nozzle height cases. For the respective cases, the volume was 75,000 mm^3, 240,000 mm^3, and 470,000 mm^3. However, it's worth noting that the crater volume data was more susceptible to camera obstructions compared to the depth data. The volume calculation requires a view of the crater walls, which is the first region to be obstructed by the ejected particles. Without view of the full crater profile, points are integrated using the coordinates of the sparse visible points.

This heightened sensitivity resulted in a shorter available duration for the volume data. The crater volume was measured to be an order of magnitude larger for the 0g cases compared to the 1g cases.

4.4 Data Curve Fitting

The crater depth from the drop tower experiments were curve fit using an arctangent function of the form $d(t) = a\arctan(bt^c)$ where d is depth,t is time, and a, b, c are curve fitting coefficients. This function was originally used to describe the crater depth growth for a two-dimensional submerged jet [54] and been used to predict the asymptotic crater depth [18]. Since the drop tower was limited in regard to test duration, the arctangent function can be used to predict the steady crater depth based on initial crater growth data. Similarly, the function can be applied to cases where depth cannot be calculated due to visual obstruction in the stereo images.

These coefficients were calculated using the MATLAB curve fitting toolbox with the constraint that these coefficients were greater than zero. The reason for positive coefficients is because they are associated with non-negative physical phenomenon such as depth, dynamic pressure, and time. Fig. 4.8 shows the curve fit and asymptotic maximum depth of Fig. 4.6. The horizontal lines represent the asymptotic depth, which asymptotes to $0.5a\pi$. It is based on the limit of the arctangent function as time approaches infinity. The dashed black lines represent the continued theoretical crater depth based on the curve fit for the specific test case.

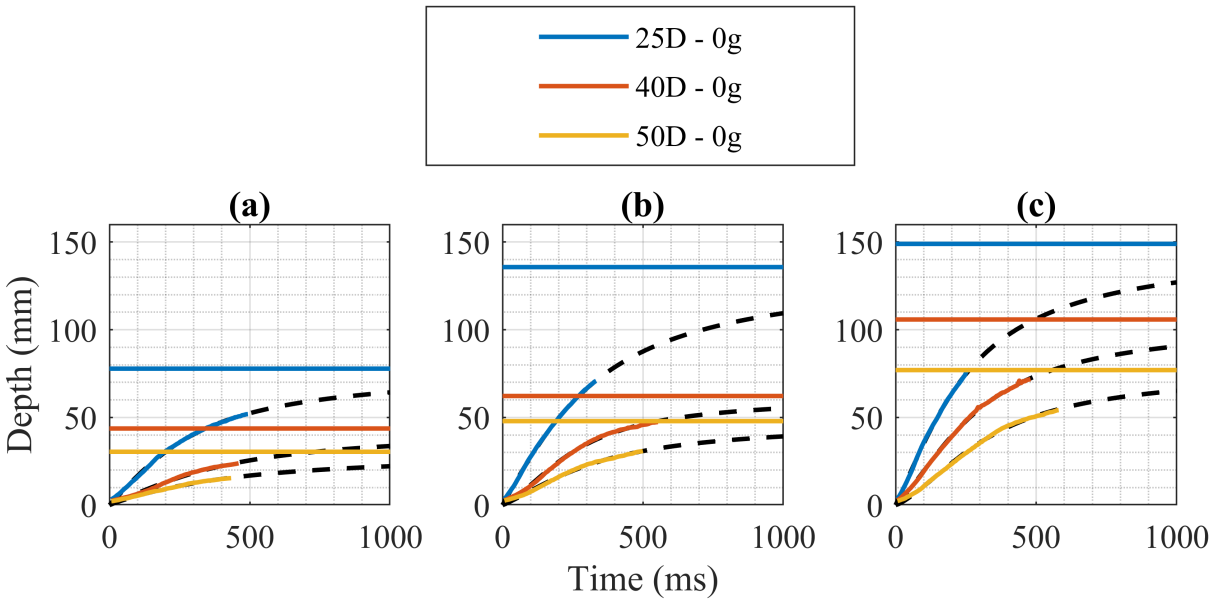

Figure 4.8: 0g Depth Extrapolation Using Arctangent Fitting function at Nozzle Pressures of (a) 5 psig (b) 10 psig (c) 15 psig

For a given nozzle height, the asymptotic depth increased for increasing nozzle pressures. In the same manner, for a given nozzle pressure, the asymptotic depth decreased for increased nozzle heights. The exact values of the predicted asymptotic depth for each drop tower case are in Table. 4.2. The asymptotic depth increased non-linearly with respect to nozzle height and nozzle pressure. As the nozzle height continues to increase, the asymptotic depth would continue to decrease until no crater forms.

Table 4.2: Drop Article Asymptotic Depth Comparison Under 0g

Nozzle Height	Nozzle Pressure (psia)	Asymptotic Depth (mm)
25	5	77.8
40	5	43.7
50	5	30.4
25	10	135.7
40	10	62.2
50	10	47.9
25	15	148.9
40	15	105.8
50	15	77.0

The a coefficient decreases for higher nozzle heights, which follows $a \propto H$ [18]. The trends of a coefficient with nozzle height are shown in Fig. 4.9 and tabulated in Table. 4.3. The coefficient of determination, R^2, was calculated based on the linear fit in Fig. 4.9. R^2 was calculated to be 0.982, 0.936, and 1.0 for the 5 psig, 10 psig, and 15 psig cases respectively. These values for R^2 indicate that the a coefficient scales linearly with nozzle height.

Low root mean square error (RMSE), between 0.15 mm and 0.71 mm, indicated that the the curve fit model is very accurate for depth prediction. These errors were the same magnitude as the error measured from the 3D-printed stair pattern. There was either not enough data or no association between nozzle height or nozzle pressure with the b and c coefficients. Metzger et al. have associated b with the jet's dynamic pressure, and both the a and b coefficient may have dependence on gravity [20]. The arctangent model works best for 0g cases to predict the initial crater growth. Although, the accuracy of asymptotic crater depth can not be concluded due to insufficient data at long time-scales. However, crater depth will not continue to grow indefinitely in 0g. The plume impingement pressure decreases at the bottom of the crater as it deepens. As the crater deepens and the impingement pressure lessens, the amount of material being removed from the crater decreases relative to the amount of material that recirculates or

avalanches back in. Eventually the impingement pressure will be too low to move the particles and erosion will cease.

(a) 0g 5 psig Coefficients

	a	b	c	RMSE
25D	49.52	3.36×10^{-3}	1.01	0.47
40D	27.81	2.21×10^{-3}	1.03	0.63
50D	19.37	4.62×10^{-3}	0.89	0.15

(b) 0g 10 psig Coefficients

	a	b	c	RMSE
25D	86.4	3.47×10^{-3}	0.99	0.35
40D	39.6	8.42×10^{-4}	1.27	0.71
50D	30.5	1.78×10^{-3}	1.09	0.56

(c) 0g 15 psig Coefficients

	a	b	c	RMSE
25D	94.8	3.24×10^{-3}	1.04	0.51
40D	67.4	1.39×10^{-3}	1.64	0.57
50D	49.0	6.62×10^{-4}	1.26	0.61

Table 4.3: Arctangent Function Coefficients and RMSE from Drop Tower Tests

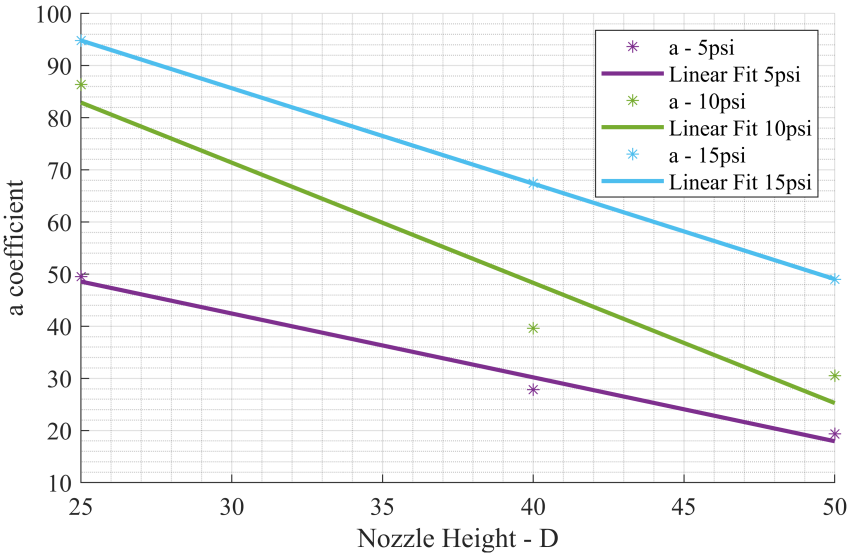

Figure 4.9: a Coefficient vs Nozzle Height for 5 psig, 10 psig, and 15 psig

To apply the arctangent fit with Earth gravity data, Fig. 4.10 shows the depth vs. time across five nozzle pressures at a nozzle height of 40D under Earth gravity. The nozzle pressures ranged from 20 psia to 40 psia. These tests were conducted in the AUCPL vacuum chamber, under Earth atmospheric conditions with the same nozzle and granular material properties listed in Table. 3.5. The tests were conducted in the vacuum chamber to compare if the depth results would be consistent across facilities. The arctangent curve fitting was applied to this dataset and was represented with dashed black lines. The fitting function was used to predict the long term crater growth based on the initial depth data from the stereo images. Based on the curve fit at 1000 ms, each increment of 5 psia nozzle pressure corresponded to an increased crater depth of approximately 10 mm. This indicated that viscous erosion occurred more rapidly as nozzle pressure increased.

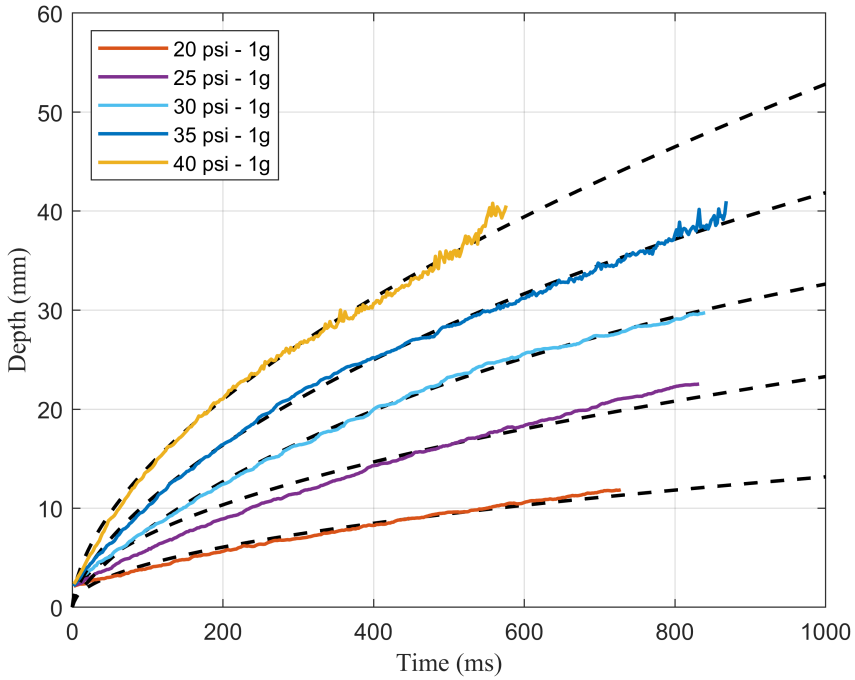

Figure 4.10: Depth vs. Time at Various Nozzle Pressures at 40D Nozzle Height Under Earth Gravity Using a Vacuum Chamber Facility

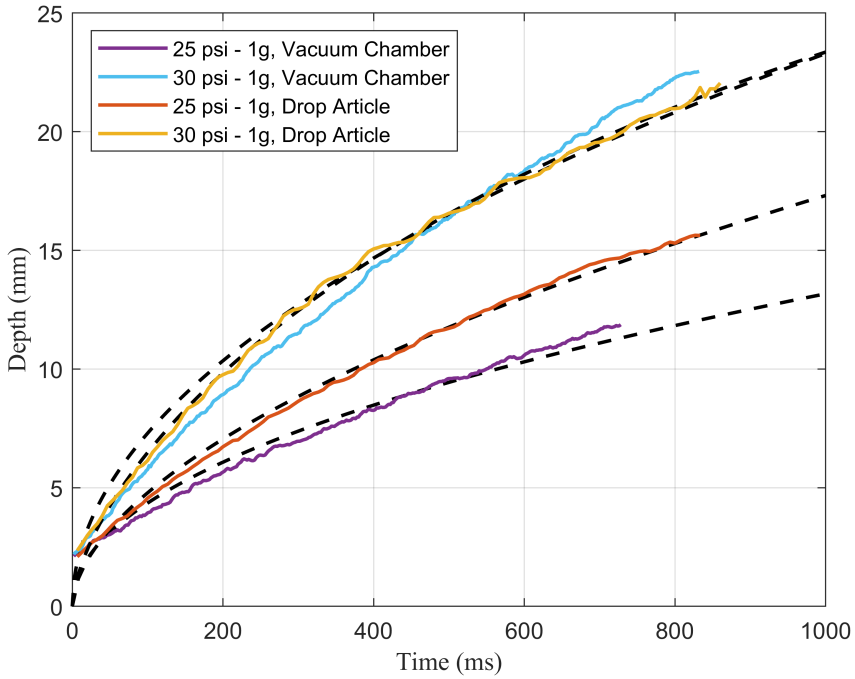

Figure 4.11: 1g Depth vs. Time at 40D, Comparing the Arctangent Fits for the Drop Article and Vacuum Chamber Facility

Fig. 4.11 compares two pressure condition cases from Fig. 4.10 that match the drop article data at at 40D nozzle height, 1g, Earth ambient pressure at 25 psia and 30 psia. The late stage crater growth for the 30 psia conditions asymptote to approximately the same depth. The

25 psia case does not follow this trend; however, this is likely due to different fanno flow effects from different hose length and material. The 30 psia case is choked, while the 25 psia case is subsonic. The difference in the subsonic velocities may be due to fanno effects or small nozzle pressure differences between the drop article and the vacuum chamber. The differences in flow velocity would cause variations in crater erosion rate. Since crater erosion rate is due to the momentum flux of the plume, a change in plume velocity would change the plume momentum that would be distributed to the sand.

4.5 Zero-G Flight Results

The ZeroG flights provided 10 Lunar, 10 Martian, and 10 Zero gravity conditions. Between each reduced gravity condition, there was a period of hyper-gravity, which was between 1g and 2g. These parabolas were flown back to back with the occasional straight and level (1g) flight approximately every 8 parabolas. Table 4.4 shows which tests were conducted during the flight, indicated by an ”x”. From this first parabolic flight, quantitative crater data was successfully recovered from 8 Martian parabolas, 5 Lunar parabolas, and none of the zero parabolas. The final two Martian parabola tests were run into existing craters, as the operator was unable to reset the sand bed at the time. Similarly, data was unable to be obtained from the remaining 5 Lunar parabolas due severe motion sickness of the experiment operators. The micro-gravity parabolas were unsuccessful from a combination of motion sickness and perturbations due to aircraft turbulence. These perturbations resulted in slightly negative gs. The small negative accelerations during the micro-gravity lofted the sand to the top plate of the flight facility, preventing any stereo measurements from the cameras. A single hyper-gravity case was conducted at a nozzle height of 25D; however, this hyper-gravity condition was 1.14g instead of the expected 1.8g. Since hyper-gravity was not the objective of the flight, there was expected variance of the hyper-gravity that may be experienced. Vibrations in the nozzle assembly were noticed during hyper-gravity pulls due to the aircraft engines and/or turbulence. These vibrations significantly reduced and were considered negligible as soon as the reduced gravity conditions were reached, and had seemingly no adverse affects on the results.

Table 4.4: Parabolic Flight 1 - PSI Test Matrix

	Lunar		**Martian**		**Zero**		**Hyper**	
	Test 1	**Test 2**	**Test 1**	**Test 2**	**Test 1**	**Test 2**	**Test 1**	**Test 2**
25D	x		x	x	x		x	
35D	x		x	x				
45D	x		x	x				
55D	x		x	x				
60D	x		x	x				

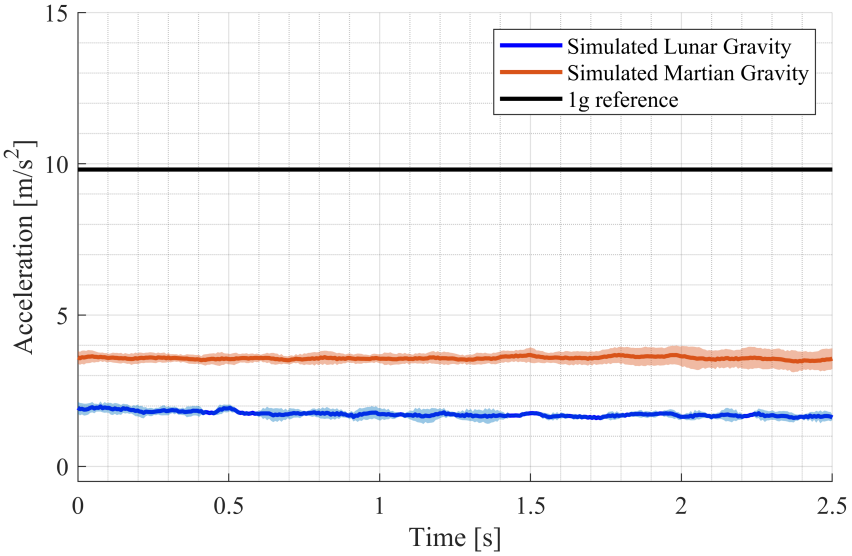

Figure 4.12: Simulated Lunar and Martian Accelerations From the Zero-G Flights

Fig. 4.12 is a plot of the simulated Lunar and Martian accelerations from the first Zero-G flight. The solid blue line is the mean Lunar acceleration across four test cases. The solid orange line is the mean Martian accelerations across all 10 Martian parabolas. The shaded region around each line represents the standard deviation of the acceleration. The time averaged mean of all Lunar accelerations was $1.72\ \frac{m}{s^2}$, and the time averaged mean of all Martian accelerations was $3.45\ \frac{m}{s^2}$. Since Lunar gravity is $1.62\ \frac{m}{s^2}$ and Martian gravity is $3.71\ \frac{m}{s^2}$, the measured gravity has an error of 6.17% for the simulated Lunar gravity and 7.01% for the simulated Martian gravity. The time averaged standard deviation for the Lunar and Martian accelerations were $0.134\ \frac{m}{s^2}$ and $0.250\ \frac{m}{s^2}$ respectively.

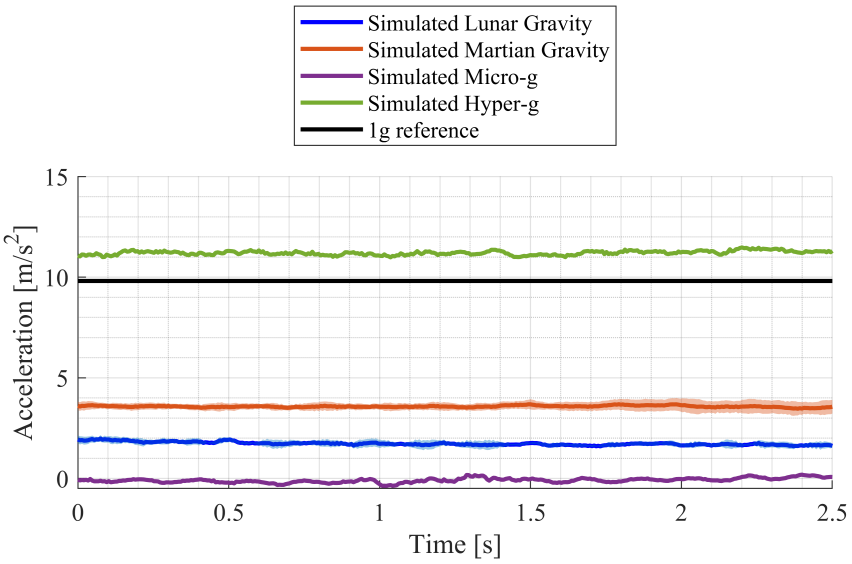

Figure 4.13: Simulated Lunar and Martian Accelerations From the Zero-G Flights

Fig. 4.13 includes the single simulated hyper-g and simulated micro-g conditions. These accelerations were recorded during the 2 second nozzle flow during each test with an additional 0.5 seconds recorded post nozzle shutoff. The time averaged hyper-g gravity case was $11.21\ \frac{m}{s^2}$ and the time averaged micro-g was $-0.06\ \frac{m}{s^2}$. The hyper-g and micro-gravity seem less "smooth" and compared to Martian and Lunar conditions since there were not multiple cases to average over.

The crater depth vs time from the parabolic flights is shown in Figs. 4.14 - 4.16. Five nozzle heights from 25D to 60D were tested at Lunar ($1.62\frac{m}{s^2}$) and Martian ($3.71\frac{m}{s^2}$) gravity conditions. The duration for each test was 2 seconds, but the data was truncated when visibility of the crater was lost. The nozzle pressures were 15.9 psig for each test. Fig. 4.14 shows the crater depth for the first set of Lunar parabolas, Fig. 4.15 shows the crater depth for the first set of Martian parabolas, and Fig. 4.16 shows the crater depth for the second set of Martian parabolas.

Similar to the drop tower experiments at 0g and 1g, the rate of crater evolution and crater depth increased with decreasing nozzle height. Visibility was lost after 125 ms for the Lunar 25D case but remained visible for the full 2000 ms duration for the Lunar and Martian 60D case. The Lunar 55D case began at a crater depth of 10 mm due to imperfect sand resetting. The second tests of Martian 55D and 60D in Fig. 4.16 were conducted into existing craters

from the previous nozzle height test because the sand was not reset. The depth did not begin asymptoting during the Lunar 25D case in Fig. 4.14. In Fig. 4.15, the 25D case overlaps with the 35D case for the first 150 ms. This does not occur again during the second Martian set in Fig. 4.16.

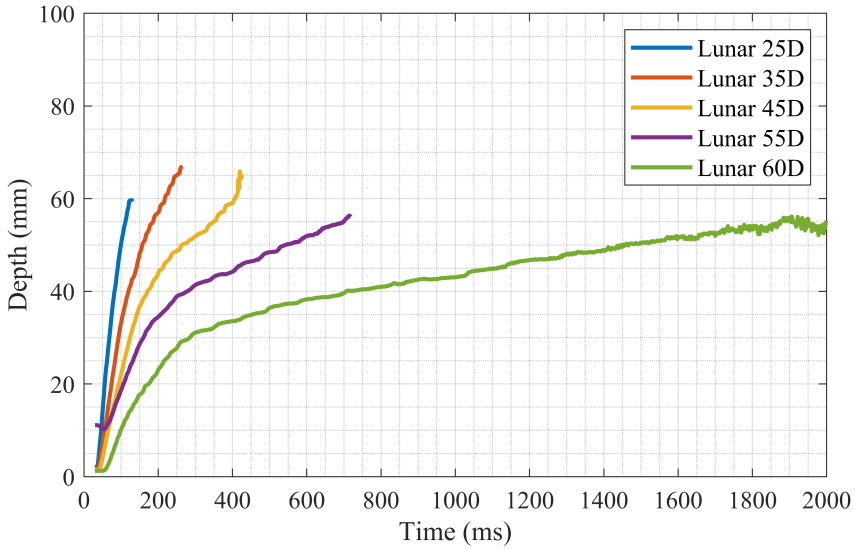

Figure 4.14: Depth vs. Time at Lunar Gravity ($1.62\frac{m}{s^2}$) at 15.9 psig Nozzle Pressure for five Nozzle Heights

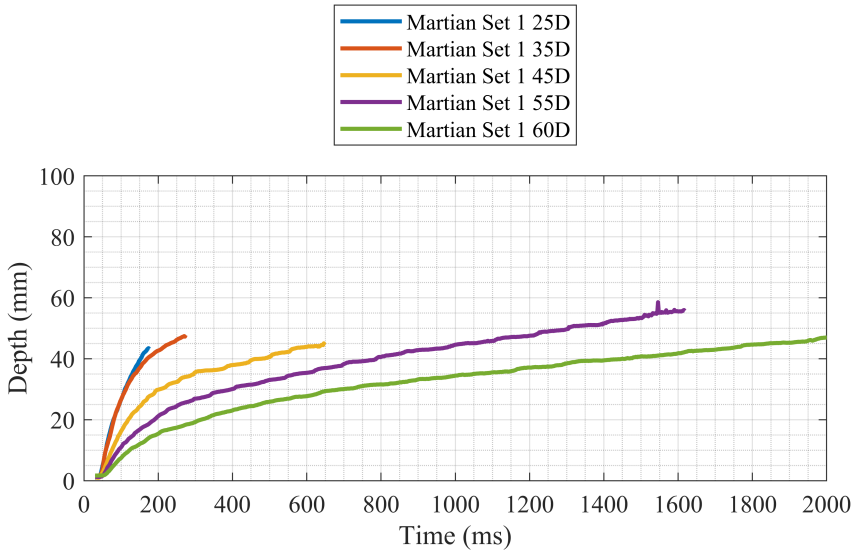

Figure 4.15: Depth vs. Time at Martian Gravity ($3.71\frac{m}{s^2}$) Set 1 for Five Nozzle Heights at 15.9 psig

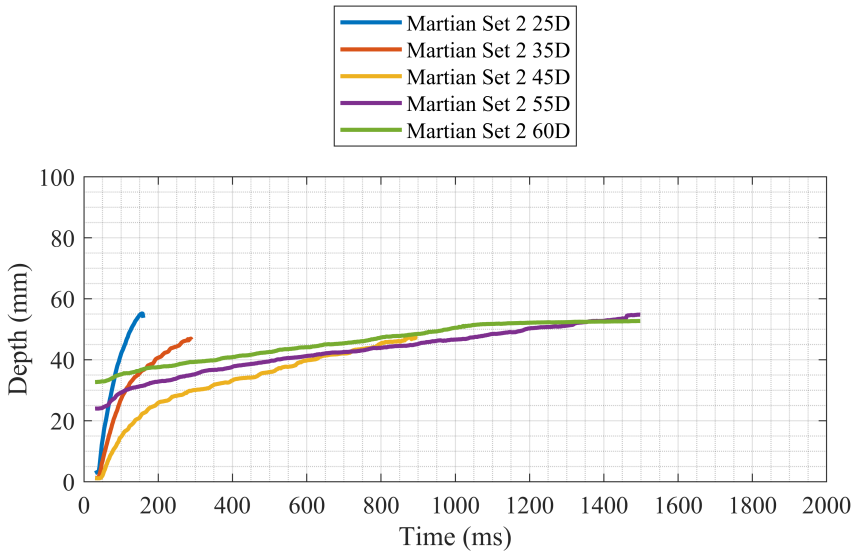

Figure 4.16: Depth vs. Time at Martian Gravity ($3.71\frac{m}{s^2}$) Set 2 for Five Nozzle Heights at 15.9 psig

Fig. 4.17 compares the two Martian depth data sets at each nozzle height. The solid lines represent the first parabola at each specific nozzle height, and the dashed line represents the second parabola at each nozzle height. The two cases appear most similar for the 35D and 45D nozzle heights. Whereas the 25D case appeared to have a different growth rate between the two tests. The 55D and 60D cannot be as easily compared together as the second tests were conducted into existing craters. The 25D case lost visual of the crater at 160 ms, the 35D at 290 ms, the 45D at 870 ms and 900 ms, and the 55D case at 1600 ms. The Martian 60D nozzle height did not lose visibility.

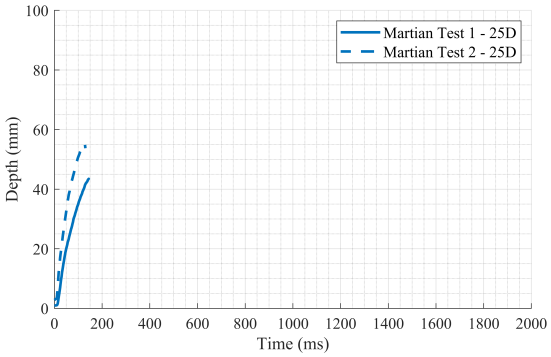

(a) Martian 25D

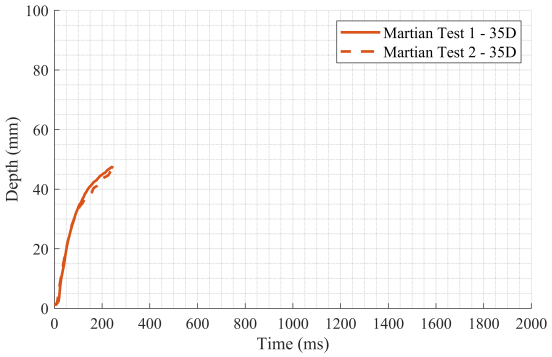

(b) Martian 35D

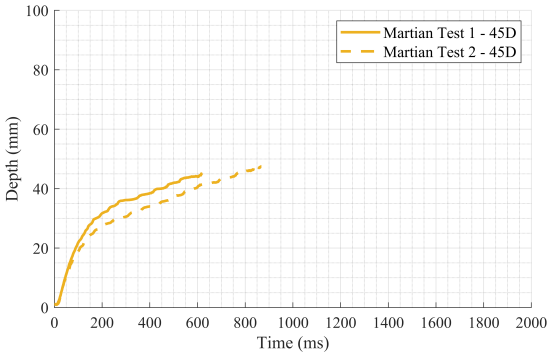

(c) Martian 45D

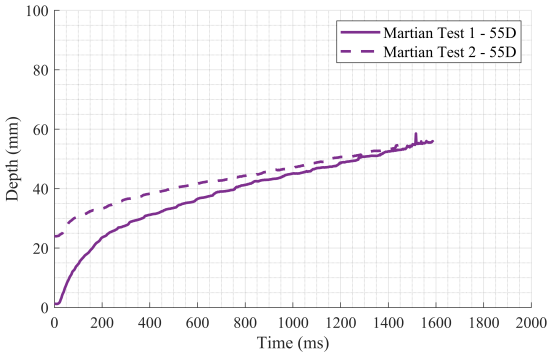

(d) Martian 55D

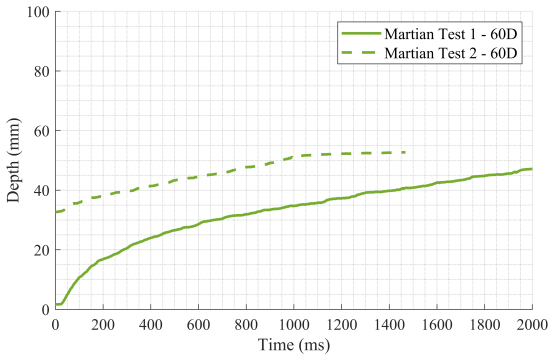

(e) Martian 60D

Figure 4.17: Depth vs. Time for Martian Nozzle Heights

The crater depths for the Martian gravity was compared to the Lunar gravity crater depths in Fig. 4.18. For each of the nozzle heights, a deeper crater depth was reached under Lunar gravity before visual obstruction occurred. The craters for the Martian gravity tests were visible for a longer duration than the Lunar gravity tests for the 25D, 45D, and 55D nozzle heights. This comparison used the second set of Martian data for the 25D, 35D, and 45D nozzle heights due to the overlap of the 25D and 35D nozzle height cases from the first set of Martian tests. The 55D and 60D tests from the first set were used in this comparison since the second set did not start at zero depth. Table. 4.5 tabulates the Lunar and Martian crater depths from Fig. 4.18 at

different time intervals and calculates the percent change from the crater depths across gravity conditions. Between 200 ms and 600 ms for the 35D, 45D, 55D, and 60D nozzle heights, the percent change across Lunar and Martian gravity was between 25.9% and 44.2%. This percent change trended lower for each nozzle height as test time progressed.

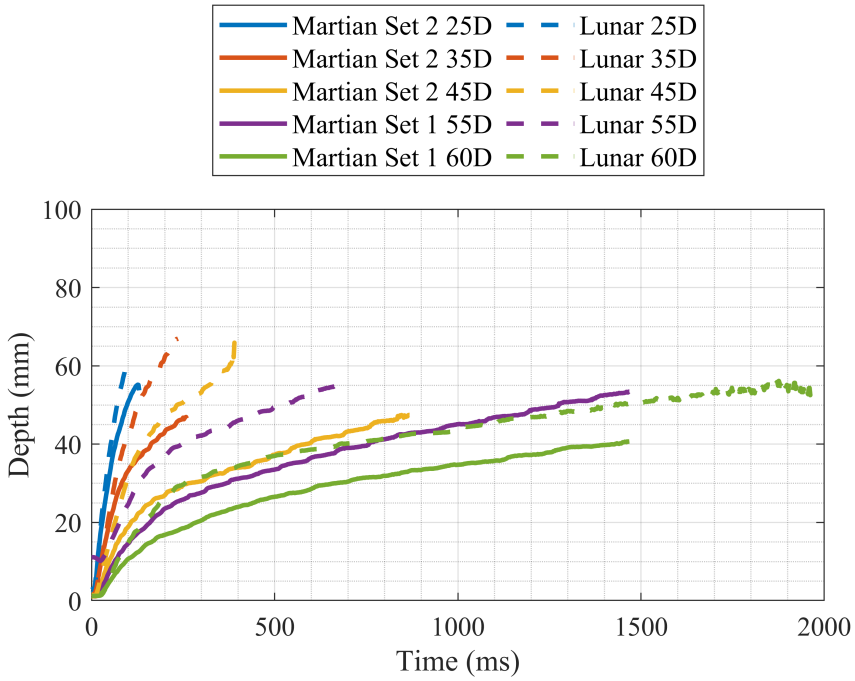

Figure 4.18: Martian Depth and Lunar Depth vs Time for Five Nozzle Heights at 15.9 psig

Table 4.5: Lunar and Martian Depth Comparison

Time (ms)	Nozzle Height	Lunar Depth (mm)	Martian Depth (mm)	Percent Change
200	35D	62.3	43.2	30.7%
200	45D	47.0	26.9	42.8%
200	55D	37.0	23.6	36.2%
200	60D	26.2	16.8	35.9%
380	45D	60.4	33.7	44.2%
400	55D	46.0	31.2	32.2%
400	60D	34.4	24.0	30.2%
600	55D	52.6	36.5	30.6%
600	60D	38.6	28.6	25.9%

To determine the cause of the depth inconsistencies between the two Martian sets in Fig. 4.17, conditions such as cabin pressure, nozzle pressure, accelerations, and camera distance were investigated. The nozzle pressure for each Martian test is shown in Fig. 4.19. Fig. 4.19 shows an initial spike in nozzle pressure, which corresponded to the opening of the solenoid valve. Following the spike, the nozzle pressure took 150 ms to reach a steady nozzle pressure of 15.9 psig. The nozzle pressure profile was nearly identical for each test. Therefore, the nozzle pressure was not attributed to the discrepancies in the depth data. The cabin pressure data, recorded from the BMP280, is shown in Fig. 4.20. The cabin pressure remained constant for each Martian test at 11.9 psia. Therefore, the variation in depth data was not caused by a variation in cabin pressure.

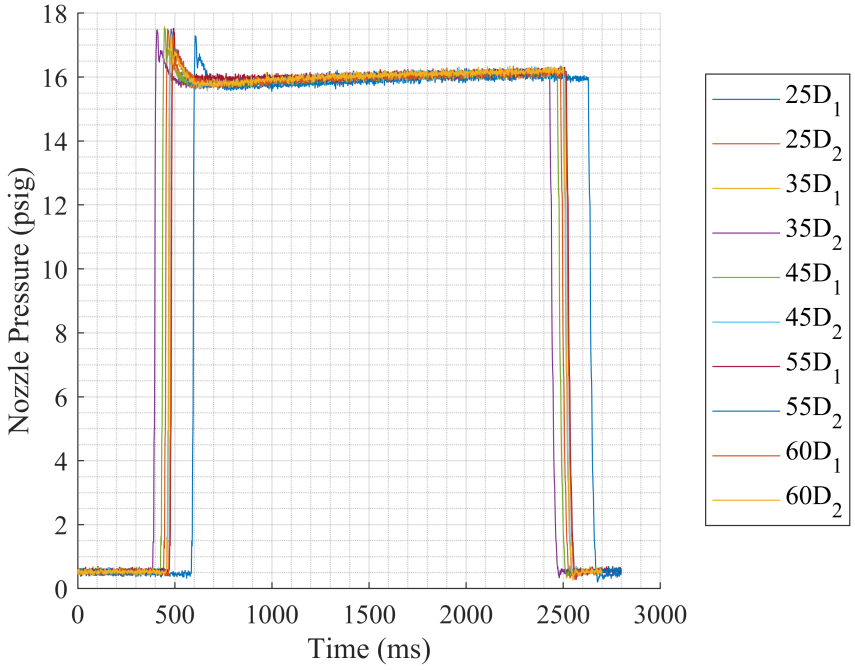

Figure 4.19: Nozzle Pressures for the Martian Cases

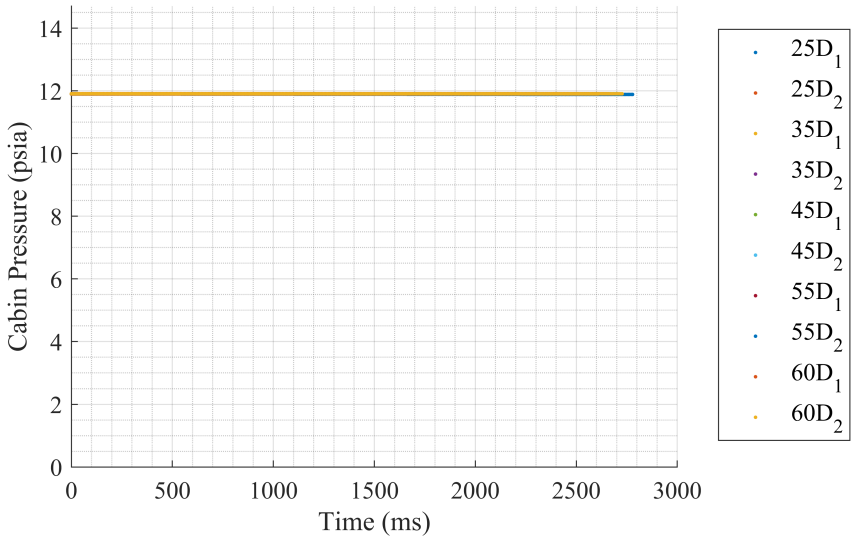

Figure 4.20: Cabin Pressures During Martian Tests

Fig. 4.21 shows a moving average of the gravitational acceleration during the two Martian 25D nozzle height tests. The second 25D Martian test had a slightly higher gravitational acceleration than the first Martian test, within $0.2\frac{m}{s^2}$. Comparing the 25D depths in Fig. 4.17a, the second test had a faster crater growth rate and increased depth. Fig. 4.21 may suggest that the increased gravity would attribute to this difference. However, the second Martian test had the increased gravitational acceleration, which would correspond to decreased crater growth rate and decreased depth. This is opposite to what is shown in Fig. 4.17a. For that reason, the differences in crater growth were not a result of the small discrepancy in the accelerations.

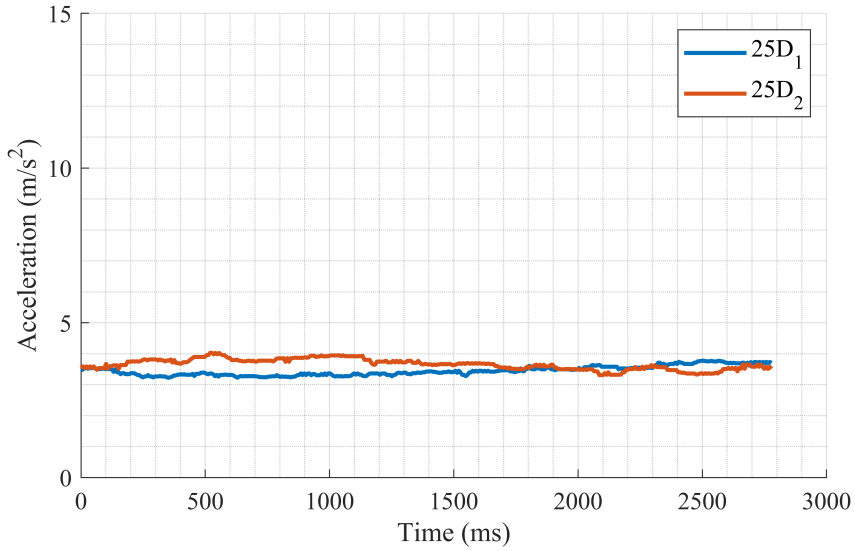

Figure 4.21: Martian Accelerations During the 25D Nozzle Height Cases

The initial point clouds for the 25D Martian cases were checked to determine if there was a difference in distance from the cameras to the sand bed. If there is a difference in the sand bed initial level, the actual nozzle height with respect to the sand surface would have changed. This would have been caused by leveling the sand surface lower or higher than the foam padded edges. The initial point clouds are shown in Fig. 4.22. Fig. 4.22 shows a top-down view of the sand surface plane. The black dot in each sub-figure indicates the center coordinate of the bed measured at the center-line of the nozzle. The z coordinate was the distance from the surface to the cameras. The distance to the cameras for the initial 25D Martian case was 895.4 mm and the distance for the second 25D Martian case was 897.2 mm. The difference in the distance from the cameras were 1.8 mm, which would not cause the difference crater growth in Fig. 4.17a. Since these factors did not deviate between tests, more repetitions are needed to determine if the inconsistencies are due to test-to-test variation.

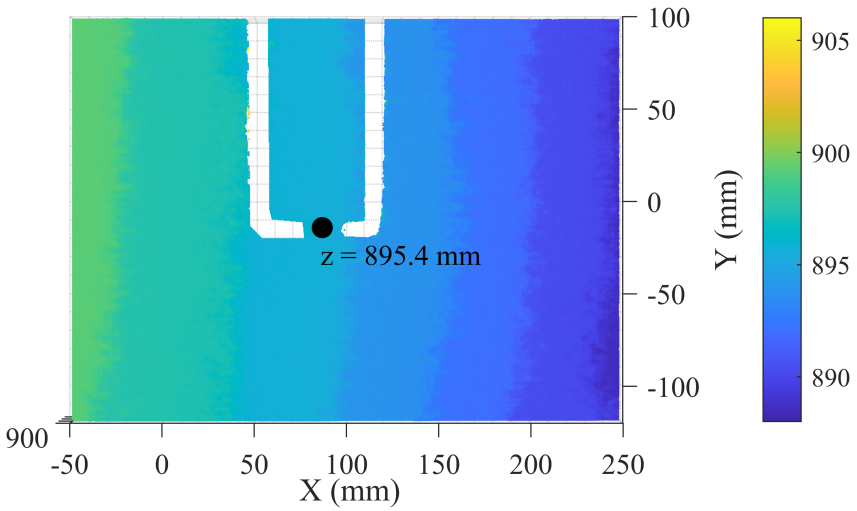

(a) Martian Test 1 25D Nozzle Height Initial Point Cloud

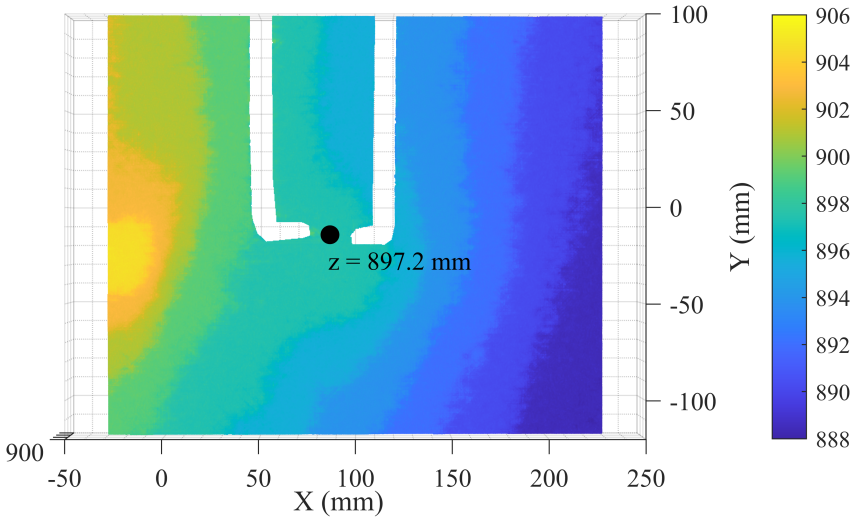

(b) Martian Test 2 25D Nozzle Height Initial Point Cloud

Figure 4.22: Initial Point Clouds for Martian 25D Nozzle Heights

The drop tower and the parabolic flight facility depth data were compared in Fig. 4.23. The Martian, Lunar, and hyper-gravity from the flight facility were compared against the 0g and 1g cases from the drop tower. nozzle height of 25D. The nozzle pressures from the flight were 15.9 psig, and the nozzle pressures from the drop tower were 15 psig. Both facilities were choked at the nozzle exit. It was expected that the crater growth rate would be higher during the 0g drops than the reduced gravity cases from the flight. Similarly the 1g tests should have a higher erosion rate than the hyper-gravity case. Discrepancies may be due to a number of factors such as the nozzle pressure difference, the sand bed depth of the drop article affecting the erosion rate, or the erosion rate behaving differently in micro-gravity. Also, the drop article

may have not yet reached the “free-fall” state before the test start, which can be mitigated by adding a short time delay starting from the drop. However, more data is needed from the parabolic flights to draw these conclusions.

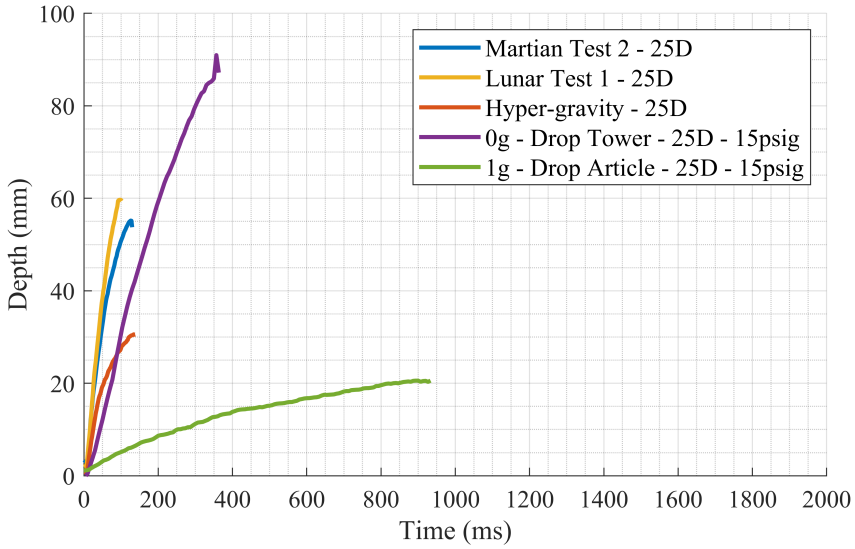

Figure 4.23: Crater Depth Measurements Using the Drop Tower and Parabolic Flight Facility at a Nozzle Height of 25D

The stereo photogrammetry technique was successfully adapted to non-intrusively measure crater formations in reduced gravity. The drop tower was used to obtain preliminary crater geometry measurements at three nozzle heights and three nozzle pressures in 1g and micro-gravity. The drop tower results showed a significant increase in crater radius under micro-gravity, while crater depth and volume increased by an order of magnitude compared to 1g conditions. Furthermore, it was observed that crater depth and volume increased with higher nozzle pressure and decreased with increasing nozzle height, for both gravity conditions. An arctangent curve fitting function was used to predict long term crater growth by fitting the initial depth data from the 1g and micro-gravity tests, and a curve fitting coefficient was identified to scale proportionally to nozzle height. Following the drop tower experiments, a parabolic flight was conducted to investigate the effect of Lunar and Martian gravity on crater formation at five nozzle heights. The reduction in gravity resulted in less resistance to viscous erosion, which caused increased crater growth rate, leading to deeper, wider, and more volumetric craters.

Chapter 5

Future Works

The objective of the drop tower experiments were to gain a preliminary understanding of the effect of reduced gravity on the crater formation process, adapt the stereo-photogrammetry technique to reduced gravity conditions, and contribute insights to inform the development of the flight facility. The effect of gravity on PSI will continue to be investigated via the remaining reduced gravity parabolic flights using the flight facility. These flights will provide reduced gravity conditions simulating Martian (0.38g), Lunar (0.16g), micro-gravity (0g), and hyper-gravity (1.8g). Introducing these other gravity conditions will improve our understanding of how gravity influences the PSI crater formation process.

New parameters will be investigated for both the drop tower and parabolic flight PSI experiments. While maintaining the existing facility designs, one avenue for investigation involves using smaller particle sizes or different granular material, such as glass beads. Higher nozzle pressures and the implementation of a converging-diverging nozzle represent another strategy for exploring higher or lower mass flow rates and cratering with a supersonic nozzle. Using smaller nozzle diameters opens up the possibility of achieving higher non-dimensional nozzle heights above the material bed. Depending on the nozzle height, nozzle pressure, and gravity, longer duration tests (longer than 2 s) should be explored. Conducting tests into existing craters may provide an avenue for obtaining crater geometry information as the crater approaches a maximum size.

The three remaining parabolic flights are planned using the flight facility. The same stereo photogrammetry technique will continue to allow for a full-domain non-intrusive measurement of the crater geometry. In these future flights, tests will be conducted at the hyper-gravity

conditions that occur between the reduced gravity components of the flight parabola. Based on the results from the first flight, longer duration tests may be needed for the higher nozzle height conditions.

5.0.1 Reduced Gravity Using the Drop Tower

Outside of the parabolic flights, reduced gravity PSI tests can be conducted by modifying the existing drop tower structure. The first modification of the drop tower to allow for a reduced gravity drop was explored by tethering the drop article to a cable braking system. This braking system uses a $\frac{1}{8}$ in steel cable connected to a roller chain. The steel cable ran through two pulleys on the top of the tower, similar to the wench cable system used in the untethered drop. The cable was connected to a roller chain that reeled onto a sprocket. There were 3D printed guards around the sprocket to help the chain reel onto itself and to prevent the chain from falling off. This sprocket was mounted onto a keyed shaft to prevent slipping. On the other end of the rod there was a braking system made from a hub, drum, and brake pad. This design required a manual reeling while the drop article was raised. This configuration for a reduced gravity drop was ultimately unsuccessful as the breaking system was unable to provide a steady constant force through the tension cable. This led to an unsteady reduced acceleration for the drops which would not be ideal for PSI experiments.

The next modification to the drop tower was a counterweight system. Using a counterweight, there is less uncertainty to the applied force on the cable as the system became a simple two-body dynamics problem. The following equations show how to determine the appropriate counterweight to achieve a target acceleration.

$$\sum F = m_{total}(g - a) \tag{5.1}$$

where a is the acceleration, g is Earth gravity, m_{total} is $m_1 + m_2$ and $\sum F = m_1 g - m_2 g$. $(g - a)$ was used to account for the acceleration needing to be calculated while also under Earth gravity. So, plug in the variables to solve for the desired acceleration.

$$a = g - \frac{m_1 g - m_2 g}{m_1 + m_2} = (1 - \frac{m_1 - m_2}{m_1 + m_2})g \tag{5.2}$$

This is the target acceleration the drop article feels during a drop. To solve for the appropriate counterweight, solve for m_2.

$$m_2 = \frac{\frac{a}{g} m_1}{2 - \frac{a}{g}} \tag{5.3}$$

Where a is the target acceleration, such as Lunar ($1.62 \frac{m}{s^2}$) or Martian ($3.71 \frac{m}{s^2}$), g is Earth gravity ($9.81 \frac{m}{s^2}$), and m_1 is the mass of the drop article ($80\ kg$). Using 5.3, the counterweight mass should be approximately 7 kg for a Lunar gravity drop and 18.6 kg for a Martian gravity drop. The next stage of drop tower experiments will conduct PSI experiments in Lunar and Martian gravity conditions at 15 psia and compare the crater geometry results with the flight facility data. If the reduced gravity drop tower provides consistent results, intermediate gravity data will not be limited to Martian or Lunar conditions from the parabolic flights. Also, the vacuum capability of the drop article will be explored to investigate the effects of both reduced atmosphere and reduced gravity on crater formation. This combination is not currently possible with the parabolic flights, as there is not enough time to pump to a vacuum condition between parabolas.

Bibliography

[1] Morris, A. B., Goldstein, D. B., Varghese, P. L., and Trafton, L. M., "Approach for modeling rocket plume impingement and dust dispersal on the moon," *Journal of Spacecraft and Rockets*, Vol. 52, No. 2, 2015, pp. 362–374.

[2] Immer, C., Metzger, P., Hintze, P. E., Nick, A., and Horan, R., "Apollo 12 Lunar Module exhaust plume impingement on Lunar Surveyor III," Vol. 211, No. 2, pp. 1089–1102.

[3] Metzger, P. T., Lane, J. E., Immer, C. D., and Clements, S., "Cratering and blowing soil by rocket engines during lunar landings," 2008.

[4] Metzger, P. T., Smith, J., and Lane, J. E., "Phenomenology of soil erosion due to rocket exhaust on the Moon and the Mauna Kea lunar test site," *Journal of Geophysical Research: Planets*, Vol. 116, No. E6, 2011.

[5] Metzger, P. T., Immer, C. D., Donahue, C. M., Vu, B. T., Latta III, R. C., and Deyo-Svendsen, M., "Jet-induced cratering of a granular surface with application to lunar spaceports," *Journal of Aerospace Engineering*, Vol. 22, No. 1, 2009, pp. 24–32.

[6] Metzger, P. T., Lane, J. E., and Immer, C. D., "Modification of Roberts' theory for rocket exhaust plumes eroding lunar soil," *Earth & Space 2008: Engineering, Science, Construction, and Operations in Challenging Environments*, 2008, pp. 1–8.

[7] Metzger, P. T., Vu, B. T., Taylor, D., Kromann, M., Fuchs, M., Yutko, B., Dokos, A., Immer, C. D., Lane, J. E., Dunkel, M. B., et al., "Cratering of Soil by Impinging Jets of Gas, with Application to Landing Rockets on Planetary Surfaces," *arXiv preprint arXiv:2104.05195*, 2021.

[8] Chambers, W. A., Dove, A. R., Cox, C. T., and Metzger, P. T., *Plume-Surface Interaction Phenomena Observed in Vacuum Microgravity*, pp. 22–31.

[9] Metzger, P. T., Lane, J. E., Immer, C. D., Gamsky, J. N., Hauslein, W., Li, X., Latta, Iii, R. C., and Donaue, C. M., "Scaling of Erosion Rate in Subsonic Jet Experiments and Apollo Lunar Module Landings," *Earth and Space 2010*, American Society of Civil Engineers, pp. 191–207.

[10] Wagner, S. A., "The Apollo Experience Lessons Learned for Constellation Lunar Dust Management," .

[11] Manned Space Center, "Apollo 17 Technical Debrief," Tech. Rep. MSC-7631, NASA, January 1973.

[12] Manned Space Center, "Apollo 11 Mission report," Tech. Rep. MSC-00171, NASA, Houston, Texas, November 1969.

[13] Manned Space Center, "Apollo 12 Mission report," Tech. Rep. MSC-01855, NASA, Houston, Texas, March 1970.

[14] Roberts, L., "The Action of a Hypersonic Jet on a Dust Layer," 1963, Paper 63-50.

[15] Roberts, L., "The Interaction of a Rocket Exhaust with the Lunar Surface (Rocket Exhaust Jet Interaction with Lunar Surface Dust Layer)," *AGARD the Fluid Dynamic Aspects of Space Flight*, Vol. 2, 1966.

[16] Roberts, L., "Visibility and Dust Erosion During the Lunar Landing," 1963.

[17] Roberts, L., "Exhaust Jet — Dust Layer Interaction During a Lunar Landing," *XIIIth International Astronautical Congress Varna 1962*, edited by N. Boneff and I. Hersey, Springer Vienna, pp. 21–37.

[18] LaMarche, C. Q. and Curtis, J. S., "Cratering of a particle bed by a subsonic turbulent jet: Effect of particle shape, size and density," Vol. 138, pp. 432–445.

[19] Haehnel, R. B., Dade, W. B., and Cushman-Roisin, B., "Crater Evolution Due to a Jet Impinging on a Bed of Loose Particles," *Earth & Space 2008*, American Society of Civil Engineers, pp. 1–10.

[20] Metzger, P. T., Latta, R. C., Schuler, J. M., Immer, C. D., Nakagawa, M., and Luding, S., "Craters Formed in Granular Beds by Impinging Jets of Gas," *AIP Conference Proceedings*, AIP, pp. 767–770.

[21] Korzun, A. M., Eberhart, C. J., West, J., Liever, P., Weaver, A., Mantovani, J., Langton, A., Kemmerer, B., and Atkins, A., "Design of a Subscale, Inert Gas Test for Plume-Surface Interactions in a Reduced Pressure Environment," *AIAA SCITECH 2022 Forum*, American Institute of Aeronautics and Astronautics.

[22] Brisset, J., Colwell, J., Dove, A., Abukhalil, S., Cox, C., and Mohammed, N., "Regolith behavior under asteroid-level gravity conditions: low-velocity impact experiments," Vol. 5, No. 1, pp. 73.

[23] Murdoch, N., Rozitis, B., Nordstrom, K., Green, S. F., Michel, P., De Lophem, T.-L., and Losert, W., "Granular Convection in Microgravity," Vol. 110, No. 1, pp. 018307.

[24] Scheeres, D., Hartzell, C., Sánchez, P., and Swift, M., "Scaling forces to asteroid surfaces: The role of cohesion," Vol. 210, No. 2, pp. 968–984.

[25] Gorman, M. T., Rubio, J. S., Diaz-Lopez, M. X., Chambers, W. A., Korzun, A. M., Rabinovitch, J., and Ni, R., "Scaling Laws of Plume-Induced Granular Cratering," *PNAS Nexus*, Vol. 2, 2023, pp. 1–8, Advance Access Publication 20 September 2023.

[26] Stubbs, D. C., Silwal, L., Thurow, B. S., Hirabayashi, M., Raghav, V., and Scarborough, D. E., "Three-Dimensional Measurement of the Crater Formation During Plume–Surface Interactions Using Stereo-Photogrammetry," *AIAA Journal*, Vol. 60, No. 3, 2022, pp. 1316–1331.

[27] Stubbs, D., Silwal, L., Bhargav, V. N., Thurow, B. S., Hirabayashi, M., Raghav, V., and Scarborough, D. E., "Non-intrusive, 3-D Crater Formation Measurements Due to Plume-Surface Interactions Under Sub-Atmospheric Pressure Conditions," *AIAA SCITECH 2023 Forum*, 2023, p. 2488.

[28] Crane, T., Stubbs, D., Thurow, B. S., Raghav, V., and Scarborough, D., "Three-Dimensional Crater Formation Measurements During Plume-Surface Interaction in a Reduced Gravity Environment Using a Drop Tower," *AIAA SCITECH 2024 Forum*, American Institute of Aeronautics and Astronautics.

[29] Romine, G., Reisert, T., and Gliozzi, J., "Site alteration effects from rocket exhaust impingement during a simulated Viking Mars landing: Part I," Tech. rep., NASA, 1973.

[30] Alexander, J., Roberds, W., and Scott, R., "Soil erosion by landing rockets Final report," Tech. rep., 1966.

[31] Land, N. S. and Conner, D. W., "Laboratory Simulation of Lunar Surface Erosion by Rockets," *Presented at the 13th Annual Institute for Environmental Sciences Technical Meeting*, NASA Langley Research Center Langley Station, Hampton, VA, 1967.

[32] Land, N. S. and Clark, L. V., "Experimental Investigation of Jet Impingement on Surfaces of Fine Particles in a Vacuum Environment," Technical Report TN D-2633, NASA, 1965.

[33] Scott, R. F. and Ko, H.-Y., "Transient rocket-engine gas flow in soil." Vol. 6, No. 2, pp. 258–264.

[34] Immer, C. and Metzger, P., "Rocket Cratering in Simulated Lunar and Martian Environments," *Earth and Space 2010*, American Society of Civil Engineers, pp. 182–190.

[35] Guleria, S. D. and Patil, D. V., "Experimental investigations of crater formation on granular bed subjected to an air-jet impingement," Vol. 32, No. 5, pp. 053309.

[36] Baba, M., Okita, S., Watanabe, K., Maru, Y., Sawai, S., Mori, O., and Fujita, K., "Microgravity Experiment using Drop Tower and CFD-DEM Coupled Simulation about Plume-Surface Interaction," *AIAA SCITECH 2023 Forum*, American Institute of Aeronautics and Astronautics.

[37] Clark, A. H. and Behringer, R. P., "Jet-induced 2-D crater formation with horizontal symmetry breaking," Vol. 16, No. 4, pp. 433–440.

[38] Tyrrell, O. K., Rodrigues, N. S., Korzun, A. M., and Danehy, P. M., "Flow visualization of intrusive and non-intrusive configurations for lunar- and Martian-relevant plume-surface interaction," *AIAA SCITECH 2024 Forum*, American Institute of Aeronautics and Astronautics.

[39] Danehy, P. M., Wilkes, J. A., Alderfer, D. W., Jones, S. B., Robbins, A., Patry, D. D., and Schwartz, R., "Planar Laser-induced Fluorescence (PLIF) Investigation of Hypersonic Flowfields in a Mach 10 Wind Tunnel (invited)," *25th AIAA Aerodynamic Measurement Technology and Ground Testing Conference*, No. 2006-3442, American Institute of Aeronautics and Astronautics, June 2006.

[40] Inman, J., Danehy, P., Nowak, R., and Alderfer, D., "The Effect of Impingement on Transitional Behavior in Underexpanded Jets," *47th AIAA Aerospace Sciences Meeting including The New Horizons Forum and Aerospace Exposition*, American Institute of Aeronautics and Astronautics.

[41] Taconet, O. and Ciarletti, V., "Estimating soil roughness indices on a ridge-and-furrow surface using stereo photogrammetry," Vol. 93, No. 1, pp. 64–76.

[42] Tran, T. V., Tucker-Kulesza, S. E., and Bernhardt-Barry, M. L., "Determining Surface Roughness in Erosion Testing Using Digital Photogrammetry," Vol. 40, No. 6, pp. 20160277.

[43] Hirschmuller, H., "Accurate and Effcient Stereo Processing by Semi-Global Matching and Mutual Information," .

[44] Hirschmuller, H., "Stereo Processing by Semiglobal Matching and Mutual Information," Vol. 30, No. 2, pp. 328–341.

[45] Schatzmann, M., "An integral model of plume rise," Vol. 13, No. 5, pp. 721–731.

[46] Kuhns, M., Metzger, P., Dove, A., Byron, J., Lamb, S., Roberson, T., Lohman, L., Chambers, W., Rixon, G., Kuhns, R., Mehta, M., and van Susante, P., *Deep Regolith Cratering and Plume Effects Modeling for Lunar Landing Sites*, pp. 62–78.

[47] Colwell, J., Brisset, J., Dove, A., Whizin, A., Nagler, H., Brown, N., Rascon, A., Brightwell, and Seward, L., "Low-Velocity Impacts into Regolith under Microgravity Conditions," *Earth and Space 2016*, American Society of Civil Engineers, pp. 81–93.

[48] Heißelmann, D., Blum, J., Fraser, H. J., and Wolling, K., "Microgravity experiments on the collisional behavior of saturnian ring particles," Vol. 206, No. 2, pp. 424–430.

[49] Colwell, J. E., Sture, S., Cintala, M., Durda, D., Hendrix, A., Goudie, T., Curtis, D., Ashcom, D. J., Kanter, M., Keohane, T., Lemos, A., Lupton, M., and Route, M., "Ejecta from impacts at 0.2–2.3 m/s in low gravity," Vol. 195, No. 2, pp. 908–917.

[50] Salter, D. M., Heißelmann, D., Chaparro, G., Van Der Wolk, G., Reißaus, P., Borst, A. G., Dawson, R. W., De Kuyper, E., Drinkwater, G., Gebauer, K., Hutcheon, M., Linnartz, H., Molster, F. J., Stoll, B., Van Der Tuijn, P. C., Fraser, H. J., and Blum, J., "A zero-gravity instrument to study low velocity collisions of fragile particles at low temperatures," Vol. 80, No. 7, pp. 074501.

[51] Colwell, J. E. and Taylor, M., "Low-Velocity Microgravity Impact Experiments into Simulated Regolith," Vol. 138, No. 2, pp. 241–248.

[52] Maurel, C., Michel, P., Biele, J., Ballouz, R.-L., and Thuillet, F., "Numerical simulations of the contact between the lander MASCOT and a regolith-covered surface," Vol. 62, No. 8, pp. 2099–2124.

[53] Balakrishnan, K. and Bellan, J., "Fluid density effects in supersonic jet-induced cratering in a granular bed on a planetary body having an atmosphere in the continuum regime," Vol. 915, pp. A29.

[54] Sarma, K., "Existence of limiting scour depth," *Journal of the Institution of Engineers (India)*, Vol. 48, No. 1, 1967, pp. 84–92.

[55] Gale, M., Mehta, R., Liever, P., Buettner, K., and Curtis, J., "Gas-Granular Flow Solver for Plume Surface Interaction and Cratering Simulations," *AIAA Aviation Forum 23rd AIAA Computational Fluid Dynamics Conference*, American Institute of Aeronautics and Astronautics (AIAA), Denver, Colorado, June 5-9 2017.

[56] Yamamoto, S., Wada, K., Okabe, N., and Matsui, T., "Transient crater growth in granular targets: An experimental study of low velocity impacts into glass sphere targets," Vol. 183, No. 1, pp. 215–224.

[57] Stubbs, D., Silwal, L., Thurow, B. S., Hirabayashi, M., Raghav, V., and Scarborough, D., "Non-intrusive, 3D Optical Measurements of Crater Formation due to Plume-Surface Interactions," *AIAA Scitech 2021 Forum*, 2021, p. 0831.